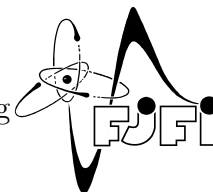




CZECH TECHNICAL UNIVERSITY IN PRAGUE  
Faculty of Nuclear Sciences and Physical Engineering



# Measurement of inclusive jet $p_T$ spectra in $p + p$ collisions at ALICE

## Měření inkluzivních $p_T$ spekter jetů ve srážkách $p + p$ na experimentu ALICE

Research task

Author: **Bc. Peter Příbeli**  
Supervisor: **RNDr. Filip Křížek, Ph.D.**  
Academic year: 2016/2017



- Zadání práce -

- Zadání práce (zadní strana) -

*Acknowledgment:*

I would like to thank Filip Křížek for his expert guidance and express my gratitude to my family for their loving support.

*Author's declaration:*

I declare that this Research Task is entirely my own work and I have listed all the used sources in the bibliography.

Prague, July 7, 2016

Peter Příbeli



*Název práce:*

**Měření inkluzivních  $p_T$  spekter jetů ve srážkách p+p na experimentu ALICE**

*Autor:* Bc. Peter Příbeli

*Obor:* Experimentální jaderná a částicová fyzika

*Druh práce:* Výzkumný úkol

*Vedoucí práce:* RNDr. Filip Křížek Ph.D., Ústav jaderné fyziky AV ČR, v.v.i.

*Abstrakt:* Práce pojednává o měření inkluzivního  $p_T$  spektra nabitých jetů ve srážkách proton-proton s  $\sqrt{s} = 13$  TeV. V úvodu se věnujeme problematice popisu tvrdých procesů ve srážkách p + p a základním principům kvantové chromodynamiky. Následně je podán popis experimentu ALICE. V analyzační části shrnujeme kritéria na výběr případů, drah částic a jetů.

*Klíčová slova:* anti- $k_T$  jet algoritmus, jet, QCD, SVD dekonvoluce, silná interakce, tvrdý proces

*Title:*

**Measurement of inclusive jet  $p_T$  spectra in p + p collisions at ALICE**

*Author:* Bc. Peter Příbeli

*Abstract:* The thesis reviews the measurement of inclusive  $p_T$  spectra of charged jets in proton-proton collisions at  $\sqrt{s} = 13$  TeV. The first part concerns the description of hard processes in p + p collisions and the basic principles of quantum chromodynamics. Then the description of the ALICE experiment is put forth. In the analysis part of the thesis the criteria for event, track and jet selection are stated.

*Key words:* anti- $k_T$  jet algorithm, hard process, jet, QCD, SVD unfolding, Strong interaction





# Contents

<b>Introduction</b>	<b>13</b>
<b>1 Hard scattering processes in p+p</b>	<b>15</b>
1.1 Cross-sections . . . . .	15
1.2 The QCD Lagrangian . . . . .	16
1.3 Elementary QCD cross-sections . . . . .	16
1.4 Asymptotic freedom . . . . .	18
1.5 Parton distribution functions . . . . .	20
1.6 Confinement . . . . .	22
1.7 Jets . . . . .	24
1.8 Background subtraction . . . . .	27
1.8.1 Standard area based approach . . . . .	28
1.8.2 CMS background . . . . .	28
1.8.3 Perpendicular cone background . . . . .	28
<b>2 Experimental setup</b>	<b>31</b>
2.1 The Large Hadron Collider . . . . .	31
2.2 A Large Ion Colliding Experiment . . . . .	31
2.2.1 Inner Tracking System (ITS) . . . . .	34
2.2.2 Time Projection Chamber (TPC) . . . . .	34
2.2.3 V0 . . . . .	34
2.2.4 Computational infrastructure . . . . .	34
<b>3 Analysis of <math>p_T</math> spectra of inclusive charged jets in p+p collisions at <math>\sqrt{s} = 13</math> TeV</b>	<b>37</b>
3.1 Event selection . . . . .	37
3.2 Track selection . . . . .	38
3.3 Jet selection . . . . .	41
3.4 Data quality assurance . . . . .	41
3.4.1 <i>2015f</i> . . . . .	41
3.4.2 <i>2016l</i> . . . . .	43
<b>4 Analysis of simulations</b>	<b>45</b>
4.0.1 Simulated events anchored to runs from <i>2016l</i> . . . . .	45
<b>5 Raw jet <math>p_T</math> spectra</b>	<b>49</b>

<b>6 Unfolding</b>	<b>53</b>
6.1 Singular Value Decomposition . . . . .	53
6.2 Response matrix . . . . .	54
6.3 Results . . . . .	55
<b>Conclusion and Outlook</b>	<b>59</b>

# List of Symbols

## Physical Constants

$\alpha_s$	The strength of the strong interaction	$\approx 1$
$\hbar$	The reduced Planck's constant.	
	$\hbar = \frac{h}{2\pi}$	$\approx 1.0546 \times 10^{-34} \text{ J s}$
$c$	The speed of light in vacuum	299, 792, 458 m/s

$g_{QCD}$  The QCD coupling constant

## Mathematical symbols

$:=$	A definition
$[A, B]$	The commutator of $A$ and $B$
$\delta_\mu^\nu$	The Dirac delta function
$\mathbb{A}^T$	The transpose of a matrix $\mathbb{A}$
$\mathbb{A}^{-1}$	The inverse of a matrix $\mathbb{A}$
$\mathbb{C}$	The set of complex numbers
$\mathbb{C}^{n,m}$	The space of complex $n \times m$ matrices
$\mathbb{N}$	The set of natural numbers
$\mathbb{R}$	The set of real numbers
$\text{diag}(x_1, x_2, \dots, x_n)$	A diagonal matrix with the values $x_1, x_2, \dots, x_n$ on its diagonal
$\text{rank}(\mathbb{A})$	The rank of the matrix $\mathbb{A}$
$\text{Tr}(\mathbb{A})$	The trace of the matrix $\mathbb{A}$
$\bar{A}$	The complex conjugate of $A$
$\cancel{X}$	The Feynman slash notation
$E[x]$	The expectation value of $x$

$f^{abc}$  The structure constants

$i$  The imaginary unit

$N(\mu, \sigma)$  The normal distribution with mean  $\mu$  and standard deviation  $\sigma$

## Other Symbols

e.g. (*exempli gratia*) For example

etc. (*et cetera*) And other things

## Physical quantities

$\eta$	The pseudorapidity
$\mathcal{L}$	The Lagrangian density
$\mu, \nu$	4-vector indices
$\phi$	The azimuthal angle
$\psi$	The bispinor
$a, b, c$	Colour indices
$A_\mu^a$	The vector (gauge) potential
$D_\mu$	The covariant derivative
$F_{\mu\nu}$	The electromagnetic field tensor
$g_{\mu\nu}$	The metric tensor
$G_{\mu\nu}^a$	The gluon field strength tensor
$J$	The angular momentum
$m$	Mass
$p_T$	The transverse momentum
$Q$	The momentum transfer of a collision
$y$	The rapidity



# Introduction

Scattering experiments played an integral part in nuclear and sub-nuclear physics. They help in the study of the structure of matter and historically yielded several fundamental discoveries. For example the discovery of the atomic nucleus by E. Rutherford and the discovery of the non-point-like character of the proton by R. Hofstadter. Furthermore, scattering experiments of electrons on protons at SLAC in the 60s revealed a rich inner structure of the proton and helped in the development of the quark model for which three physicists—Jerome I. Friedman, Henry W. Kendall and Richard E. Taylor—won the 1990 Nobel Prize. A significant milestone in the understanding of hadrons was the discovery of Quantum Chromodynamics (QCD) and its subsequent integration with the parton model.

The de Broglie wavelength of particles shortens as their momentum increases which allows to get better spatial resolution. The Large Hadron Collider at CERN, at present the largest particle accelerator in the world, allows the study of the structure of the proton in a kinematic region which has never been explored so far. Hard processes between interacting partons can reveal interesting information about the proton at small Bjorken  $x$  values. In the final state of a hard scattering where quarks and gluons are involved one can usually find a collimated showers of high energy particles the so-called jets. In principle, by assigning the particles to a jet one can gain more information about the final state parton. The assignment of particles to jets is often ambiguous because it is not clear whether a particle belongs to a jet or not. Therefore many jet algorithms have been developed and nowadays they provide a consistent connection between the theoretical and experimental results. Apart from the useful information that jets convey about the inner structure of the proton, jets serve as an efficient tool in the study of the Quark Gluon Plasma (QGP). Understanding jet production in elementary processes is crucial for these measurements.

The aims of this thesis are:

- The understanding of QCD, hard processes, fragmentation and jets
- The description of the ALICE experiment
- The analysis of measured, uncorrected jet spectra with the selection of appropriate data files based on the observation of the stability of parameters
- The study of background accompanying the production of jets
- The determination of the response matrix of the detector
- The unfolding of charged jet  $p_T$  spectra.



# Chapter 1

## Hard scattering processes in $p+p$

During relativistic proton collisions in the LHC, the interaction usually takes place on the level of fundamental constituents—quarks and gluons. The description of this interaction is provided by QCD.

Quantum chromodynamics (QCD) [1] is the accepted fundamental theory of the strong interaction describing the interaction between particles possessing the colour charge, quarks and gluons. QCD is a non-abelian quantum field theory invariant under local  $SU(3)_c$  gauge transformations.

The basic concepts of QCD shall be outlined in the subsequent chapters and the following conventions shall be used in this chapter. The units are fixed such that the speed of light and the reduced Planck's constant are  $c = 1$ ,  $\hbar = 1$ . Greek indices  $(\mu, \nu, \dots)$  denote elements of a 4-vector. Latin indices  $(a, b, \dots)$  are used to denote colour degrees of freedom unless explicitly stated otherwise. A repeated index invokes the Einstein summation rule where an implicit summation is taken over the repeated index. Furthermore, the Feynman slash rule is used  $\not{A} := \gamma^\mu A_\mu$  where  $\gamma^0, \gamma^1, \gamma^2, \gamma^3$  are Dirac matrices.

### 1.1 Cross-sections

At present it is impossible to compute cross-sections of a hard interaction of composite objects like protons or neutrons solely from basic principals. A cross-section of an interaction such as  $p + p \rightarrow h + X$ , where  $X$  stands for all possible final states has to be calculated phenomenologically [2]. The interaction of a composite object is decomposed into three temporally distinct phases. The initial internal structure of the incoming composite particles before the collision is encompassed in the *parton distribution functions* which describe the distribution of quarks and gluons inside the proton long before the interaction occurs. Then an elementary interaction which is calculable from QCD takes place. The elementary process is of short duration and does not affect a *hadronization* phase that occurs long after the interaction. This factorization is summarised as

$$\sigma_{A+B \rightarrow h+X} = \sum_{a,b,c,d} \int dx_1 dx_2 f_{a/A} \cdot f_{b/B} \cdot \sigma_{a+b \rightarrow c+d} * D_{h/c}, \quad (1.1)$$

where  $\sigma_{A+B \rightarrow h+X}$  is the cross section of the interaction of two composite objects  $A$  and  $B$  containing partons  $a$  and  $b$  respectively,  $f_{i/I}(x, Q^2)$  are parton distribution functions of the parton  $i$  in the composite object  $I$  dependent on the fraction of the momentum carried by the parton  $x$  and the energy scale  $Q^2$ ,  $\sigma_{a+b \rightarrow c+d}$  is the elementary cross section of partons  $a+b \rightarrow c+d$

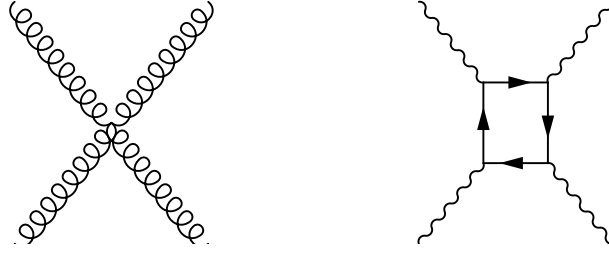


Figure 1.1: **Left:** Gluon self interaction in QCD is allowed in the lowest perturbative order. **Right:** Lowest order diagram of  $\gamma\gamma$  scattering. The scattering is enabled by means of a fermion loop.

and  $D_{h/c}(z, p_T)$  is the fragmentation function of parton  $c$  that yields the hadron  $h$  carrying the fraction  $z$  of the original parton energy and the transverse momentum  $p_T$ . The sum over all combination of partons  $a, b, c$  and  $d$  is taken and  $*$  signifies further integration over the momenta  $p_c$  and  $p_d$  that lead to the final state [2]. All of these terms shall be examined further.

## 1.2 The QCD Lagrangian

The Lagrangian density of QCD is [1]

$$\mathcal{L}_{QCD} = \sum_{\text{flavour}} \bar{\psi} (i\mathcal{D} - m) \psi - \frac{1}{4} G_{\mu\nu}^a G_a^{\mu\nu}, \quad (1.2)$$

where  $\psi$  is a 4-component Dirac spinor,  $\mathcal{D} := \gamma^\mu D_\mu = \gamma^\mu (\partial_\mu + ig_{QCD} A_\mu^a T_a)$  is the covariant derivative of QCD,  $\bar{\psi} := \psi^\dagger \gamma^0$  is the Dirac conjugate of  $\psi$ ,  $G_{\mu\nu}^a := \partial_\mu A_\nu^a - \partial_\nu A_\mu^a - g_{QCD} f^{abc} A_\mu^b A_\nu^c$  is the gluon field strength tensor,  $g_{QCD}$  is the coupling constant of the strong interaction and  $T_a$  are the generators of the colour  $SU(3)$  group under which the local gauge transformation  $\psi \rightarrow e^{-i\alpha(x)^a T_a} \psi$ ,  $a \in \{1, \dots, 8\}$  holds while the gluon field  $A_\mu^a$  also transforms.

The peculiar nature of QCD is well demonstrated by a comparison with QED. For this purpose, consider the QED Lagrangian density [1]

$$\mathcal{L}_{QED} = \bar{\psi} (i\mathcal{D} - m) \psi - \frac{1}{4} F_{\mu\nu} F^{\mu\nu}, \quad (1.3)$$

where  $F_{\mu\nu}$  is the electromagnetic field strength tensor defined as  $F_{\mu\nu} = \partial_\mu A_\nu - \partial_\nu A_\mu$  and  $A_\mu$  is the electromagnetic 4-potential, i.e. the photon field. Analogously to QED, the gluon field strength tensor  $G_{\mu\nu}^a$  describes the dynamics of the gluon field  $A_\mu^a$ . However, it has an extra term. Since gluons carry colour degrees of freedom, in contrast to photons which do not possess the electromagnetic charge, the term  $g_{QCD} f^{abc} A_\mu^b A_\nu^c$  results in gluon self interactions. Thus interactions of the kind seen in Fig. 1.1 (Left) are physically allowed, whereas photon self interactions are not allowed in the leading order of QED. In higher orders of perturbation photons can e.g. interact via a fermion loop shown in Fig. 1.1 (Right).

## 1.3 Elementary QCD cross-sections

Using the QCD Lagrangian (1.2) one can calculate various elementary cross-sections  $\sigma$  which enter (1.1). For example, Table 1.1 presents spin averaged, leading order invariant amplitudes



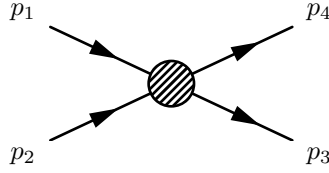


Figure 1.2: The scheme of a particle interaction. 4-momenta of incoming particles are denoted  $p_1$  and  $p_2$ , 4-momenta of outgoing particles are labelled as  $p_3$  and  $p_4$ .

for basic  $2 \rightarrow 2$  processes of unpolarized quarks, antiquarks and gluons. Quarks and antiquarks are assumed massless. Here  $s, t, u$  denote Mandelstam variables which are defined as

$$s = (p_1 + p_2)^2, \quad (1.4)$$

$$t = (p_1 - p_4)^2, \quad (1.5)$$

$$u = (p_1 - p_3)^2, \quad (1.6)$$

where  $p_1, p_2, p_3$  and  $p_4$  are 4-momenta of particles involved in the  $2 \rightarrow 2$  interaction defined in Fig. 1.2.

Process	$\frac{ \overline{\mathcal{M}} ^2}{g^4}$
$qq' \rightarrow qq'$	$\frac{4}{9} \frac{s^2 + u^2}{t^2}$
$\bar{q}q' \rightarrow \bar{q}q'$	$\frac{4}{9} \frac{s^2 + u^2}{t^2}$
$qq \rightarrow qq$	$\frac{4}{9} \left( \frac{s^2 + u^2}{t^2} + \frac{s^2 + t^2}{u^2} \right) - \frac{8}{27} \frac{s^2}{ut}$
$\bar{q}q \rightarrow \bar{q}'q'$	$\frac{t^2 + u^2}{s^2}$
$\bar{q}q \rightarrow \bar{q}q$	$\frac{4}{9} \left( \frac{s^2 + u^2}{t^2} + \frac{t^2 + u^2}{s^2} \right) - \frac{8}{27} \frac{u^2}{st}$
$\bar{q}q \rightarrow gg$	$\frac{32}{27} \frac{u^2 + t^2}{ut} - \frac{8}{3} \frac{u^2 + t^2}{s^2}$
$gg \rightarrow \bar{q}q$	$\frac{1}{6} \frac{u^2 + t^2}{ut} - \frac{8}{3} \frac{u^2 + t^2}{s^2}$
$qq \rightarrow qq$	$-\frac{4}{9} \frac{u^2 + s^2}{ut} + \frac{u^2 + s^2}{t^2}$
$gg \rightarrow gg$	$\frac{9}{2} \left( 3 - \frac{ut}{s^2} - \frac{us}{t^2} - \frac{st}{u^2} \right)$

Table 1.1: Elementary QCD cross sections of different  $2 \rightarrow 2$  processes at the leading order [3].

The angular distribution can be obtained from the Mandelstam variables  $u$  and  $t$  as

$$t = -\frac{1}{2}s(1 - \cos \theta), \quad (1.7)$$

$$u = -\frac{1}{2}s(1 + \cos \theta), \quad (1.8)$$

where  $\theta$  is the scattering angle in the centre-of-mass system. The elementary invariant amplitudes as functions of  $\cos \theta$  are plotted in Figure 1.3. The mid-rapidity region<sup>1</sup> is located around  $\cos \theta = 0$ . Note that for some processes the forward-backward asymmetry is apparent, e.g.  $\bar{q} + q \rightarrow \bar{q} + q$ .

<sup>1</sup>The central barrel of the ALICE experiment covers the pseudorapidity range  $|\eta| < 0.9$ , which corresponds to an approximate scattering angle interval  $\theta \in (44^\circ, 136^\circ)$  or  $\cos \theta \in (-0.7, 0.7)$ .

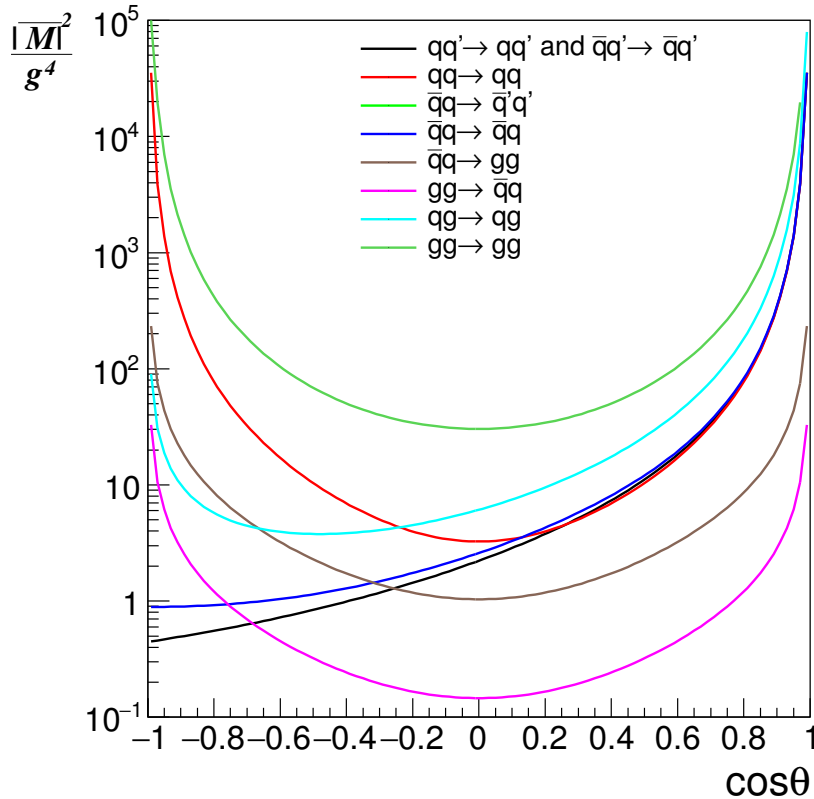


Figure 1.3:  $\frac{|\mathcal{M}|^2}{g^4}$  plotted for different 2 body processes as given in Table 1.1.

## 1.4 Asymptotic freedom

The size of the coupling in QCD,  $g_{QCD} = \sqrt{4\pi\alpha_s}$  depends on the transferred 4-momentum. For large momentum transfers the QCD coupling decreases to zero—a phenomenon known as *asymptotic freedom* [4]. For small momentum transfers the coupling diverges. This behaviour of the coupling can be explained as follows. In QED, free charges are surrounded by a cloud of virtual fermion anti-fermion pairs arising from vacuum. This is known as vacuum polarisation and is responsible for the screening of the electric charge [2]. This leads to a notion of an effective charge—the net charge of the particle and its surrounding cloud of particle anti-particle pairs.

The screening effect is also present in QCD. However, the fact that gluons possess colour degrees of freedom introduces a new phenomenon—anti-screening. Virtual gluons can be created from vacuum and enhance the net colour charge and therefore affect the coupling strength. The change in the coupling strength due to screening effects is known as the running of the coupling constant [2].

One can quantify the running of the coupling constant by the  $\beta$ -function which is derived from the renormalization group [4], [5]. The derivation shall be carried out in the subsequent text. Consider an observable  $F(Q^2)$  dependent on the energy scale  $Q^2$ . Renormalisation introduces a new energy scale  $\mu$ . Since the observable  $F(Q^2)$  only depends on one parameter, defining  $\alpha_s \equiv F(\mu^2)$  as a measurable renormalised coupling constant will fully determine the renormalised theory.

The renormalization of the perturbative expansion of  $F(Q^2)$  must not depend on the renormalization scale  $\mu$  meaning that fixing a different value of  $\alpha_s' \equiv F(\mu'^2)$  must yield the same renormalization of  $F(Q^2)$ . This independence of the renormalization procedure on the renormalization scale is called the group condition.

The introduction of a renormalization scale  $\mu$  and the group condition leads to a differential equation for  $\mu$

$$\mu^2 \frac{d}{d\mu^2} F\left(\frac{Q^2}{\mu^2}\right) = 0 \Leftrightarrow \left[ \mu^2 \frac{\partial}{\partial \mu^2} + \mu^2 \frac{\partial \alpha_S}{\partial \mu^2} \frac{\partial}{\partial \alpha_S} \right] F\left(\frac{Q^2}{\mu^2}\right) = 0. \quad (1.9)$$

Introducing  $\tau = \ln\left(\frac{Q^2}{\mu^2}\right)$  and  $\beta(\alpha_S) = \mu^2 \frac{\partial \alpha_S}{\partial \mu^2}$  gives

$$\left[ -\frac{\partial}{\partial \tau} + \beta(\alpha_S) \frac{\partial}{\partial (\alpha_S)} \right] F\left(\frac{Q^2}{\mu^2}\right) = 0. \quad (1.10)$$

Solving the differential (1.10) yields an expression for  $\beta(\alpha_S)$ . Consider

$$\frac{\partial F}{\partial \tau} = \beta(\alpha_S) \frac{\partial F}{\partial \alpha_S} \Leftrightarrow \frac{1}{\beta(\alpha_S)} \frac{\partial \alpha_S}{\partial F} = \frac{\partial \tau}{\partial F}, \quad (1.11)$$

multiplying the last equation by the Jacobian  $\frac{\partial F}{\partial \alpha_S}$  gives

$$\frac{1}{\beta(\alpha_S)} = \frac{\partial \tau}{\partial \alpha_S} \Leftrightarrow \int_0^{\alpha_S(Q^2)} d\tilde{\alpha}_S \frac{1}{\beta(\tilde{\alpha}_S)} + C = \int_0^{\alpha_S(Q^2)} d\tilde{\alpha}_S \frac{\partial \tau}{\partial \tilde{\alpha}_S} = \tau. \quad (1.12)$$

Equation (1.10) has no initial or boundary conditions and therefore has a class of functions as its solution (signified by an arbitrary constant  $C$ ). A concrete solution is chosen from the class by fixing  $C$ . In this case, it is convenient to shift the lower limit of integration to a known value by picking  $C \equiv \int_{\alpha_S(\mu^2)}^0 d\tilde{\alpha}_S \frac{1}{\beta(\tilde{\alpha}_S)}$ . The chosen solution to equation (1.10) is thus expressed as a function of the upper limit of the integral

$$\tau = \ln\left(\frac{Q^2}{\mu^2}\right) = \int_{\alpha_S(\mu^2)}^{\alpha_S(Q^2)} d\tilde{\alpha}_S \frac{1}{\beta(\tilde{\alpha}_S)} \quad (1.13)$$

The  $\beta$ -function can now be expressed perturbatively in powers of  $\alpha_S$  as

$$\beta(\alpha_S) = \sum_{n=0}^{+\infty} \beta_n \alpha_S^n. \quad (1.14)$$

where  $\beta_0 = \beta_1 = 0$ . At a one-loop order the equation becomes

$$\beta_2 \ln\left(\frac{Q^2}{\mu^2}\right) = \int_{\alpha_S(\mu^2)}^{\alpha_S(Q^2)} d\tilde{\alpha}_S \frac{1}{\tilde{\alpha}_S^2(Q)} = \frac{1}{\alpha_S(\mu^2)} - \frac{1}{\alpha_S(Q^2)}. \quad (1.15)$$

and thus

$$\alpha_S(Q^2) = \frac{\alpha_S(\mu^2)}{1 - \beta_2 \alpha_S(\mu^2) \ln\left(\frac{Q^2}{\mu^2}\right)}. \quad (1.16)$$

For the one-loop expansion in QED  $\beta_2 = \frac{1}{3\pi}$  and in QCD  $\beta_2 = -\frac{11N_c - 2N_f}{12\pi} = -\frac{7}{4\pi}$ , where  $N_c = 3$  is the number of colours and  $N_f = 6$  is the number of flavours. In QED,  $\beta_2$  is positive and

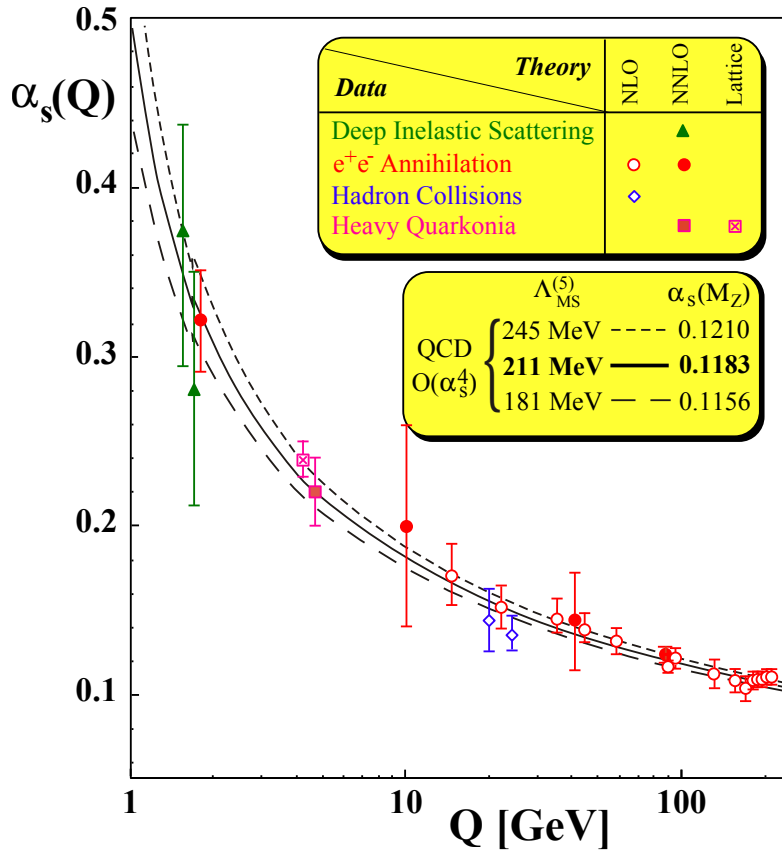


Figure 1.4: Measurement of the running of the strong coupling constant  $\alpha_s$ . The solid line is a theoretical prediction. Points represent experimentally determined values. The point with the square marker with an "X" has been obtained from non-perturbative lattice QCD. Taken from [6].

thus the coupling increases with larger  $Q^2$ . On the other hand in QCD  $\beta_2$  is negative and the coupling decreases with increasing  $Q^2$ .

Equation (1.16) describes the running of the coupling constant with  $Q^2$ . The fact that

$$\lim_{Q^2 \rightarrow \infty} \alpha_s(Q^2) = 0, \quad (1.17)$$

represents *asymptotic freedom*— the higher the energy (shorter probe wavelength) the weaker the strong coupling appears to be. The behaviour of  $\alpha_s$  can be seen in Figure 1.4.

## 1.5 Parton distribution functions

A parton distribution function  $f_{i/I}(x, Q^2)$  gives the probability distribution of finding a parton with flavour  $i$  in the given hadron carrying a fraction  $x$  of the total hadron momentum having the squared 4-momentum transfer of the hard interaction  $Q^2$  [7]. Parton distribution functions are measured using deep inelastic scattering of leptons on nucleons [2]. The presumption that electrons and neutrinos have no internal structure is utilised. The current knowledge of the parton distribution functions of a proton is shown in Figure 1.5. The plot shows separately the distribution of valence quarks  $u$  and  $d$  and the distribution of gluons (labelled  $g$ ) and sea quarks

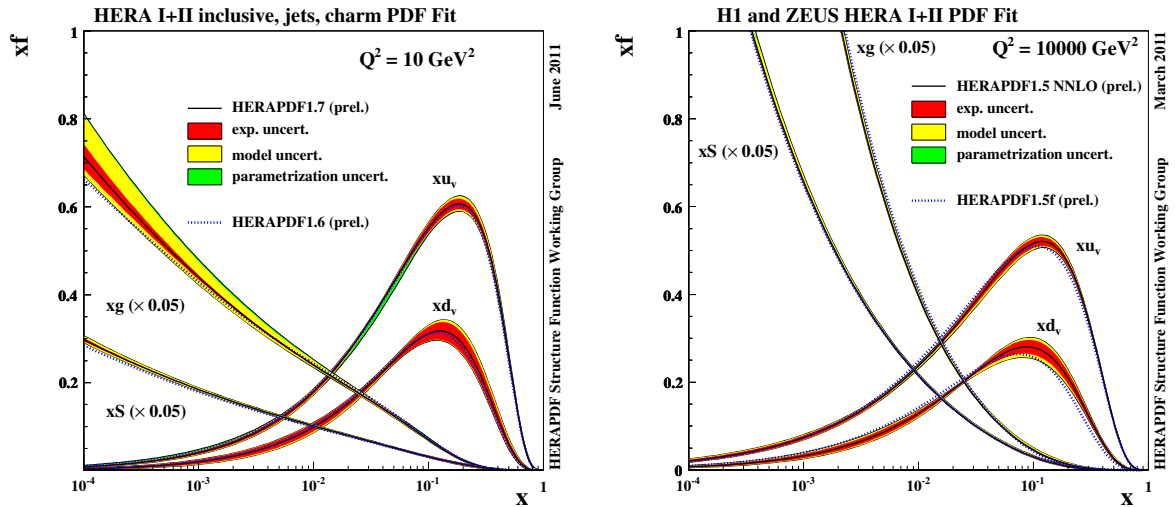


Figure 1.5: The (proton) parton distribution functions from HERAPDF1.7 at  $Q^2 = 10 \text{ GeV}^2$  **Left** and  $Q^2 = 10000 \text{ GeV}^2$  **Right**. The gluon and sea distributions are scaled down by a factor 20. The experimental, model and parametrisation uncertainties are shown separately. For comparison, the central values of HERAPDF1.6 are also shown [7].

(labelled as  $S$ ). Note, that the parton distribution functions are plotted scaled by  $x$ . At large  $x$ , parton distribution functions are dominated by valence quarks, and the measured maxima of the valence quark distribution well reflect the constituent quark composition of the proton.

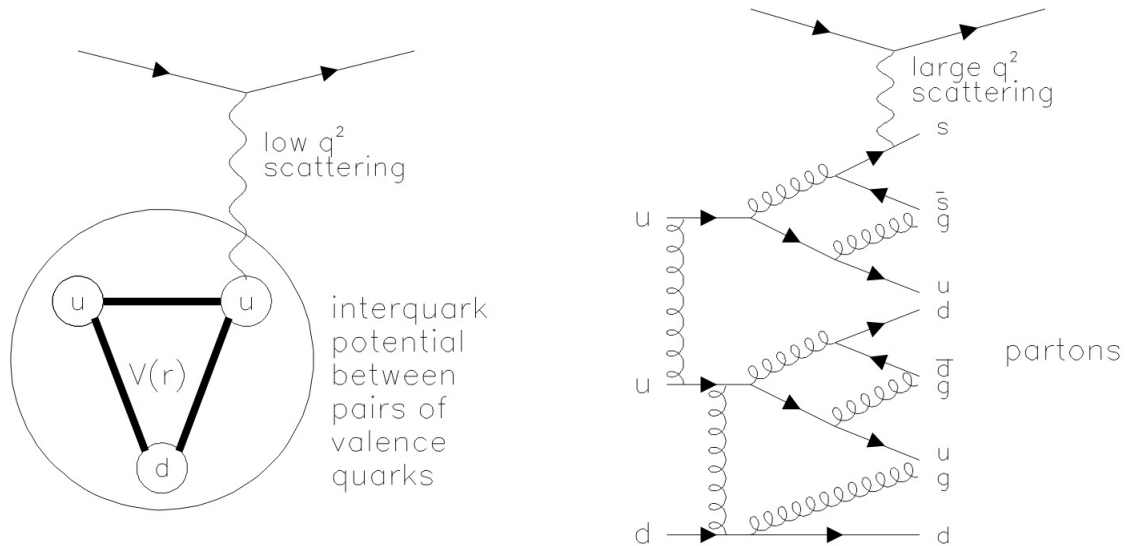


Figure 1.6: The proton structure as probed at different  $Q^2$ . **Left:** A lepton scattering on a proton at low  $Q^2$ . **Right:** A lepton scattering on a proton at high  $Q^2$ . Taken from [2].

The proton picture is dependent on the wavelength by which it is observed. When a proton is observed at low resolution, for example with a low  $Q^2$  electron scattering, it behaves as three

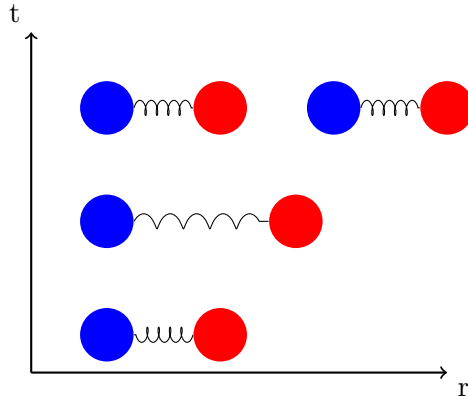


Figure 1.7: QCD colour confinement in the string model. Two quarks with a string are pulled apart. The potential energy in the string increases until a pair of virtual particles is created from vacuum which restores the colour neutrality of the original object.

valence quarks bound by a static potential as depicted in the left part of Figure 1.6. On the other hand, a hard process can distinguish a virtual particle—anti-particle pair that has been created from a gluon. The sea quarks are all virtual particles and must annihilate in a short amount of time given by the Heisenberg uncertainty relations. If the  $Q^2$  is high the probe (lepton) will most likely scatter on a virtual particle (see Figure 1.6 right) [2]. The proton is therefore dominated by sea quarks at high resolutions.

The Relativistic Heavy Ion Collider can accelerate protons to  $\sqrt{s} = 200$  GeV and is therefore dominated by  $q + q$  processes whereas the LHC accelerates protons to  $\sqrt{s} = 14$  TeV and is dominated by  $g + g$  processes [3].

## 1.6 Confinement

Fragmentation functions give the probability that after an interaction quark  $q$  is in the hadron  $h$  with transverse momentum  $p_T$  and carries the fraction  $z$  of its energy. Thus these functions phenomenologically describe the probability of the transition of an object with colour charge to a colour-neutral state and reflect *colour charge confinement* [2].

The colour charge confinement is a feature of QCD postulating that no colour charge can exist in an isolated state. Although the detailed quantitative understanding of colour confinement is still an open question, it is supported by the extensive lack of observations of any isolated colour charges.

Historically various phenomenological models that describe confinement of quarks in hadrons have been developed. The MIT Bag model [8] is used to describe quarks in stationary (non-perturbative regime of QCD) hadrons. It assumes that the quarks are massless objects in a bag. Confinement arises with the introduction of the inward bag pressure  $B$  which is balanced by the kinetic energy of the quarks inside the bag. It can be shown [8] that the bag pressure is related to the number of particles in the bag  $N$  and the size of the bag  $R$  as

$$B^{\frac{1}{4}} = \left( \frac{2.04N}{4\pi} \right)^{\frac{1}{4}} \frac{1}{R}. \quad (1.18)$$

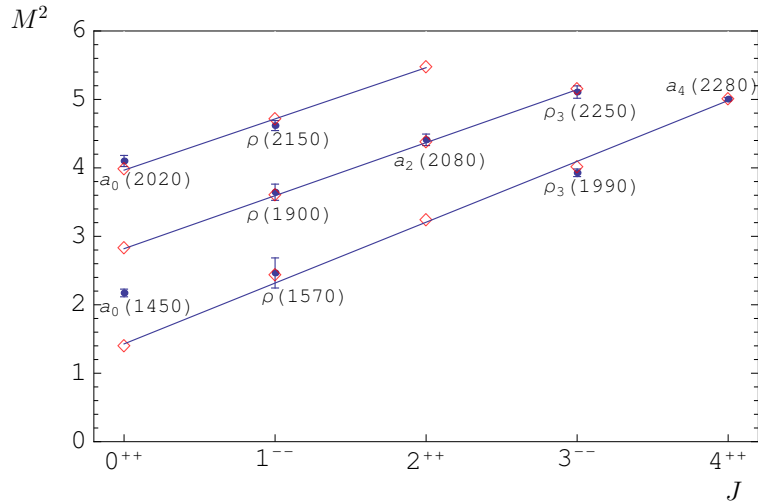


Figure 1.8: Parent and daughter  $(J, M^2)$  Regge trajectories for isovector light mesons with natural parity ( $\rho$ ). Diamonds are predicted masses. Available experimental data are given by dots with error bars and particle names.  $M^2$  is in  $\text{GeV}^2$  [9].

The confinement radius for a 3 quark system can be taken as  $R = 0.8$  fm to yield the value of the bag pressure  $B^{\frac{1}{4}} = 206$  MeV, which is consistent with the experimental limits  $145 \text{ MeV} < B^{\frac{1}{4}} < 235$  MeV [8].

A simple Bag model however, is not suitable for the description of the dynamics of the colour confinement in hadronization. A more suitable model [8] envisions the field between quarks as a colour string. The gluon self-interaction restricts the colour field into strings between individual quarks in a hadron. To model the colour string between quarks, the effective QCD potential can be introduced in the form

$$V_{QCD}^{\text{eff}} = -\frac{4}{3} \frac{\alpha_S}{r} + kr, \quad (1.19)$$

where  $r$  is the distance and  $k \sim 1$  GeV/fm is the string tension. This potential is obtained from excited states of quarkonia and supported by the existence of Regge trajectories in hadron spectra. Regge trajectories are experimentally observed dependencies of square mass  $M^2$  and spin  $J$  of hadron resonances. Hadron resonances with identical internal symmetry quantum numbers but different spins lie on a trend where  $M^2$  is a linear function of  $J$  [8], see Figure 1.8 which shows the Regge trajectories for  $\rho$  mesons. Confinement in the perturbative regime is modelled using this linear string potential  $kr$ .

Consider a particle—anti-particle pair connected by a colour string. The pair of bound particles oscillates in a so-called yo-yo mode. When trying to separate these two bound quarks by transferring energy to them, the potential energy in the hypothetical string grows with increasing distance until it prompts the creation of a particle—anti-particle pair from vacuum as depicted in Figure 1.7. Thus two strings are formed which leads to the production of hadrons and the restoration of the colour neutrality of the  $q\bar{q}$  giving rise to the confinement of the colour charge.

The Lund model [3] gives the probability distribution of the locations of the vertices at which the string is broken. The vertices lie approximately on the constant proper time world line [8]. The worldlines of the interacting particles and the subsequent breaking of the string into new particles with their worldlines are illustrated in Figure 1.9.

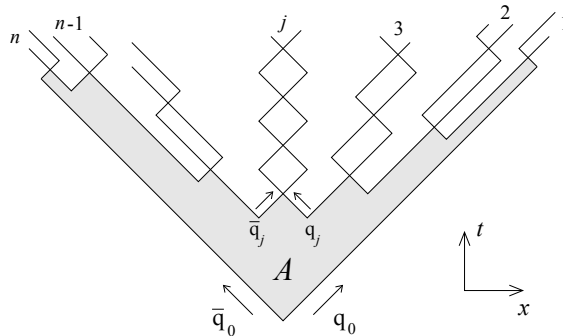


Figure 1.9: The break-up in space-time of a Lund colour string into  $n$  hadrons. The fragmentation area is denoted by  $A$  [10]. The rectangles correspond to yo-yo modes of quark strings in the produced hadrons. The area of a closed yo-yo cycle corresponds to the produced particle's mass.

Thus when two partons interact via a hard process the phenomenon of confinement leads to the production of new particles—*fragmentation*. It is the result of the restoration of the colour neutrality of the interacting partons. Therefore hard processes with quarks and gluons in the final state are characteristic by the production of showers of particles in the form of jets. Gluons carry more colour charge than quarks and therefore generally fragment to more particles than quarks [1].

Fragmentation remains poorly understood from the first principles of QCD and the use of phenomenological models such as the Lund model is needed in order to simulate the final state of hard interactions. The Lund model is implemented in the widely used Monte Carlo generator PYTHIA [11].

## 1.7 Jets

A phenomenon that arises with hard scattering processes with a quark or a gluon in the final state is the formation of collimated high energy particle showers that originated in hadronization. These showers are called *jets*. The hadronization phase obscures the information about the initial hard scattering process. Historically the determination of the 4-momentum of the hadron shower has been attempted in order to reconstruct the kinematics of outgoing scattered partons. This however cannot be done unambiguously and the concept of a phenomenological jet has been introduced. While jets have a theoretical foothold in QCD only a phenomenological definition is utilized henceforth.

A jet is defined by an heuristic algorithm—the jet algorithm that clusters individual final state hadrons. The jet algorithm reassembles the 4-momenta of all the final state hadrons in the shower and thereby extracts information about the original parton that led to the formation of the jet. The two algorithms that are further utilized are the  $k_T$  and anti- $k_T$  algorithms.

- **The  $k_T$  algorithm** is a sequential recombination algorithm [12]. The following metrics are used in the  $k_T$  algorithm for hadron collisions when grouping particles into a jet

$$d_{ij} = \min(p_{T i}^2, p_{T j}^2) \frac{\Delta R_{ij}^2}{R^2}, \quad \Delta R_{ij}^2 = (y_i - y_j)^2 + (\phi_i - \phi_j)^2, \quad (1.20a)$$

$$d_{iB} = p_{T i}^2, \quad (1.20b)$$



where  $p_T$ ,  $y$  and  $\phi$  are the transverse momentum, rapidity and the azimuthal angle respectively. The first metric (1.20a) is a metric concerning two particles  $i$  and  $j$  whereas metric (1.20b) is a metric between particle  $i$  and the beam. The  $k_T$  algorithm first computes all the metrics then if  $d_{ij}$  is smaller than  $d_{iB}$  particles  $i$  and  $j$  are combined into a pseudojet and the metrics are calculated again. Note that the term particle is used for both real particles and pseudojets alike. If  $d_{iB}$  is smaller than every  $d_{ij}$  it declares the pseudojet  $i$  as a jet and removes it from the set of particles and the metrics are computed again. This procedure is iterated until no particles remain in the set. Note that the concept of a pseudojet is a purely algorithmic construct and can be thought of as a collection of particles. The  $k_T$  algorithm starts the clusterization of particles with the softest ones.

- **The anti- $k_T$  algorithm** follows [12] an identical procedure as the  $k_T$  algorithm only the metric is changed to

$$d_{ij} = \min(p_{T_i}^{-2}, p_{T_j}^{-2}) \frac{\Delta R_{ij}^2}{R^2}, \quad \Delta R_{ij}^2 = (y_i - y_j)^2 + (\phi_i - \phi_j)^2, \quad (1.21a)$$

$$d_{iB} = p_{T_i}^{-2}. \quad (1.21b)$$

Both the  $k_T$  and the anti- $k_T$  algorithms satisfy the essential conditions on a jet algorithm namely infrared (IR) and collinear safety which are essential for the correspondence between phenomenological jets and QCD jets. *Infrared safety* means that the radiation of an IR gluon must not change the particle configuration of jets. *Collinear safety* means that the collinear splitting of particles must not change the configuration of jets. IR and collinear safety are illustrated in Figures 1.10 and 1.11 respectively.

The necessity of these conditions is illustrated by the spectrum of gluons emitted in a  $q \rightarrow qg$  process. The differential spectrum of a quark radiating a gluon in the leading order is given by [13]

$$dw^{q \rightarrow qg} = \frac{2\alpha_S(k_T^2)}{3\pi} \left[ 1 + \left( 1 - \frac{k}{E} \right)^2 \right] \frac{dk}{k} \frac{dk_T^2}{k_T^2}, \quad (1.22)$$

where  $k^\mu$  is the 4-momentum of the radiated gluon,  $E$  is its energy,  $k$  its longitudinal momentum and  $k_T$  its transverse momentum. This spectrum exhibits an infrared divergence at  $k \rightarrow 0$  and a collinear divergence at  $k_T \rightarrow 0$ . The emitted gluons would therefore mostly have a small energy and would be emitted in the forward direction meaning that the emitted gluons would be preferentially collinear and soft. However, in the next-to-leading order these divergences cancel with the contribution from loop diagrams and the cross section remains finite. This is due to the Kinoshita-Lee-Nauenberg/Block-Nordsieck theorem [14] which states that soft and collinear divergences cancel between real and virtual diagrams at any given order of the perturbation theory.

To get a consistent relation between observables in the theory and experiment this cancellation must be preserved and therefore the observable has to be insensitive to collinear branchings and soft emissions. Therefore the jet reconstruction algorithms have to be infrared and collinear safe in order to yield finite cross sections.

Both the  $k_T$  and the anti- $k_T$  algorithm are implemented in the *FastJet* package [15]. One of the difference between the  $k_T$  and the anti- $k_T$  algorithms lies in the shapes of the jet. *FastJet* determines the shape of the jet area by an addition of very soft particles called *ghost particles* which are discussed in the following chapter. The anti- $k_T$  algorithm produces more rounded jets

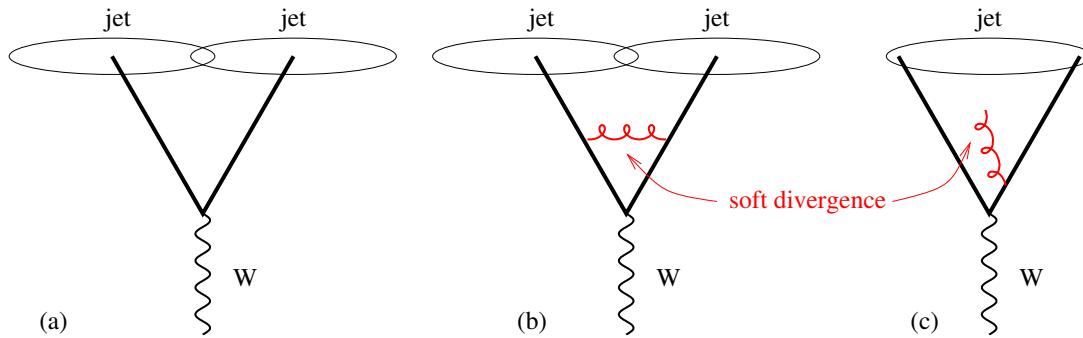


Figure 1.10: Infrared unsafety of jet algorithms. Picture a) shows the initial definition of jets. The emission of a soft gluon has converted the event from having two jets to just one jet [12].

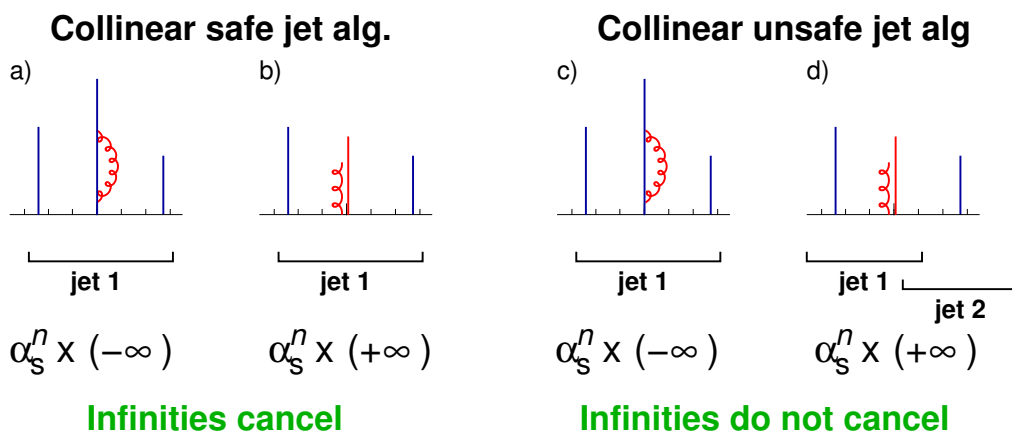


Figure 1.11: Collinear safety of jet algorithms. Pictures a) and b) illustrate collinearly safe algorithms where the emission of a collinear gluon does not change the definition of a jet whereas pictures c) and d) illustrate collinearly unsafe algorithms [12].

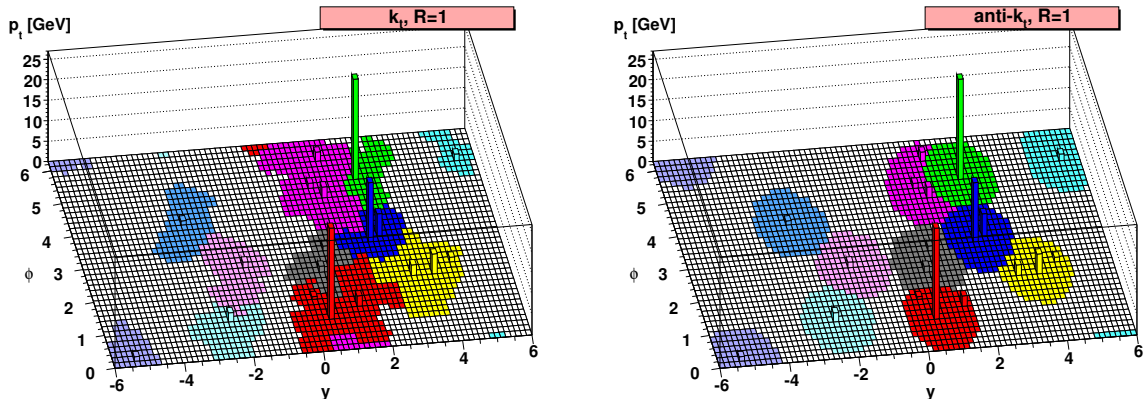


Figure 1.12: The comparison of the rapidity-azimuthal distributions of jets for the **Left**:  $k_T$  and the **Right**: anti- $k_T$  algorithms [12].

than the  $k_T$  algorithm. This is shown in Figure 1.12. Furthermore, the  $k_T$  algorithm prefers to cluster low  $p_T$  particles first as opposed to the anti- $k_T$  algorithm which is apparent from their metrics definitions (1.20) and (1.21). This is used in jet analyses of heavy-ion collisions where it is difficult to distinguish a jet from a soft background. In this case, it is convenient to start building jets from the hardest particles because hard particles could have originated only in a hard scattering. On the other hand, the background is dominated by soft particles.

## 1.8 Background subtraction

Jets originate from hard parton-parton scatterings in particle collisions. The products of a hard scattering is accompanied by the so called underlying event [16] which encompasses particles produced by other processes during the collision and which are believed to be uncorrelated with the hard scattering process. An example of such a process is the colour neutralisation of projectile remnants or a multi-parton interaction. The spectrum of underlying event particles is much softer. The soft part is considered to be a background from the jet's perspective. Various methods for correcting jet  $p_T$  spectra for soft background effects have been devised.

The correction to the  $p_T$  of the jets is done on an event-by-event basis where the corrected jet  $p_T$  spectrum is

$$p_T^{\text{jet}} = p_{T,\text{rec}}^{\text{jet}} - A^{\text{jet}} \rho, \quad (1.23)$$

where  $p_{T,\text{jet}}^{\text{rec}}$  is the uncorrected jet  $p_T$ ,  $A^{\text{jet}}$  is the jet area and  $\rho$  is the medium background density per unit area. This method of background subtraction thus introduces two new parameters [17]. The first one represents the susceptibility of a jet to contamination by a soft background. This is embodied in the parameter called the *jet area*  $A^{\text{jet}}$ . Jets, as defined in the sections above, are composed of point-like objects and thus have no area. A jet area is therefore defined by introducing infinitely soft (negligible  $p_T$ ) —*ghost particles*. Ghost particles have a definite area thus when they are clustered by the jet algorithm to a jet, they define its area. Note that IR safety is crucial in this procedure because the ghost particles must not change the composition of real jets. The jet area can vary significantly from the intuitive area of a cone jet equal to  $\pi R^2$  [18]. It depends on the jet algorithm used as well as on the individual composition of each jet. The second parameter is the medium background  $p_T$  density per unit area  $\rho$  which can be estimated by various methods. The standard area based approach, its modification by the

CMS collaboration and a perpendicular cones method are described further. The background can only be removed on average. The jet  $p_T$  is corrected, according to (1.23), only for mean background. This correction does not account for the local fluctuations in the background which further smear the jet  $p_T$ . These effects need to be corrected by unfolding.

As mentioned before, the preferred jet algorithm for the clusterisation of background jets is the  $k_T$  algorithm because it clusters soft particles first and is therefore more sensitive to the soft background. Thus the standard area based and CMS approaches to the  $\rho$  estimation operate on  $k_T$  jets.

### 1.8.1 Standard area based approach

In this method, the background density is estimated based on the observation that the ratio of the jet transverse momentum  $p_T^{\text{jet}}$  and the jet area  $A^{\text{jet}}$  behaves in two distinct ways for hard and soft jets. For hard jets, the ratio  $\frac{p_T^{\text{jet}}}{A^{\text{jet}}}$  is large compared to soft jets where the ratio is close to  $\rho$  [18]. Therefore the medium background density is estimated as

$$\rho = \text{median}_{i \in N} \left\{ \frac{p_{T,i}^{\text{jet}}}{A_i^{\text{jet}}} \right\}, \quad (1.24)$$

where  $N$  is the set of all jets in an event.

This method underestimates the background in sparsely populated events such as a  $p + p$  collision since the median can be dominated by contributions of ghost-particle jets for which  $p_T^{\text{jet}}$  is zero. It is therefore convenient to pick a large  $R$  parameter in order for the median to be non-zero.

### 1.8.2 CMS background

In light systems such as the  $p + p$  collision with a low average charged-particle multiplicity, large parts of the detector do not contain physical jets and are covered only by ghost jets. In the standard area based method, ghost jets contribute to the background density as  $\frac{p_{T,i}}{A_i} = 0$  and events with a majority of ghost jets have zero  $\rho$ . This is corrected in [19] by modifying (1.24) to

$$\rho^{\text{CMS}} = \text{median}_{i \in M} \left\{ \frac{p_{T,i}^{\text{jet}}}{A_i} \right\} \cdot \frac{A^{\text{phys}}}{A^{\text{all}}}, \quad (1.25)$$

where  $A^{\text{phys}}$  is the area covered by physical jets only and  $A^{\text{all}}$  is the area covered by all jets. Physical jets are jets with at least one real particle. Furthermore, the median is constrained to physical jets  $M$  only.

### 1.8.3 Perpendicular cone background

Another method that can be used to estimate the local  $p_T$  background density is based on the  $p_T$  density in cones that are perpendicular to the leading jet in azimuth. First the leading jet (jets with the highest  $p_T$ ) in an event is found. Then, two cones perpendicular to the leading jet in azimuth and with the same pseudorapidity are constructed. This approach is based on the assumption that the region defined by the perpendicular cones is expected to be occupied by very few particles directly correlated with the leading jet. In a  $2 \rightarrow 2$  process the resulting jets

are expected to be balanced in azimuth due to the conservation of momentum. The background is then given by

$$\rho^{\text{cone}} = \frac{p_{\text{T}}^{\text{sum}}}{2\pi R^2}, \quad (1.26)$$

where  $p_{\text{T}}^{\text{sum}}$  is the summed  $p_{\text{T}}$  of all tracks that fall into the two cones and  $R$  is the radius of the cones. The area of the cones has to be chosen large enough, typically  $R$  can be set to 0.4. This method may overestimate the background in case of an event with more than two correlated jets, like a  $2 \rightarrow 3$  process, and in the case that the jets are not precisely balanced in azimuth due to the intrinsic jet  $k_{\text{T}}$  [3]. This method is also more sensitive to the local fluctuations of the underlying event because it only studies a restricted part of the whole event.

The comparison of  $\rho$  of the three aforementioned approaches for p+p collisions at  $\sqrt{s} = \text{TeV}$  is shown in section 3.3.



## Chapter 2

# Experimental setup

### 2.1 The Large Hadron Collider

The **Large Hadron Collider** [20] is a particle accelerator located at the European Organisation for Nuclear Research (CERN) in Geneva Switzerland. The LHC is the world's largest circular accelerator. It accelerates protons and lead nuclei in ultrahigh vacuum in two beams in opposite directions. These beams cross at four places with four large experiments (ATLAS, ALICE, CMS, LHCb) built around these interaction points. Particles are guided through the ring using superconducting electromagnets cooled by superfluid helium to 1.9 K. The beam pipes cross at four interaction points where large experiments have been built to observe the collisions. The LHC was built for better understanding unsolved questions in high energy physics by colliding particles at unprecedented energies and luminosities.

The acceleration of protons in the LHC is a multi-step process consisting of several stages [21]. First, an electric discharge removes the electron from hydrogen atoms leaving only hydrogen nuclei—protons. These are then accelerated in a linear accelerator *Linac 2* which accelerates them to 50 MeV. The protons are then injected into the *Proton Synchrotron Booster*— a circular accelerator that accelerates them to 1.4 GeV. The chain continues with the *Proton Synchrotron* and the *Super Proton Synchrotron* which accelerate the protons to 25 GeV and 450 GeV respectively. The Super Proton Synchrotron then injects the particles into the LHC which as of 2017 accelerates protons to a maximum energy of 6.5 TeV. The accelerator chain is depicted in Figure 2.1.

### 2.2 A Large Ion Colliding Experiment

**A Large Ion Colliding Experiment** is an experiment located at the 2nd interaction point of the LHC. Its main purpose is the study of Quark Gluon Plasma— a state of matter created in high energy heavy physics ion collisions. Besides the heavy-ion program, ALICE has a rich pp program.

ALICE consists of a central barrel and a forward muon arm. The central barrel is placed in the *L3* magnet which supplies a 0.5 T magnetic field. The interaction point is situated in the centre of the central barrel. The detectors surrounding the interaction point are dedicated to track reconstruction and identify the outgoing particles. The three detectors that are of importance to this analysis shall be discussed further. The schematic depiction of ALICE is in Figure 2.2.

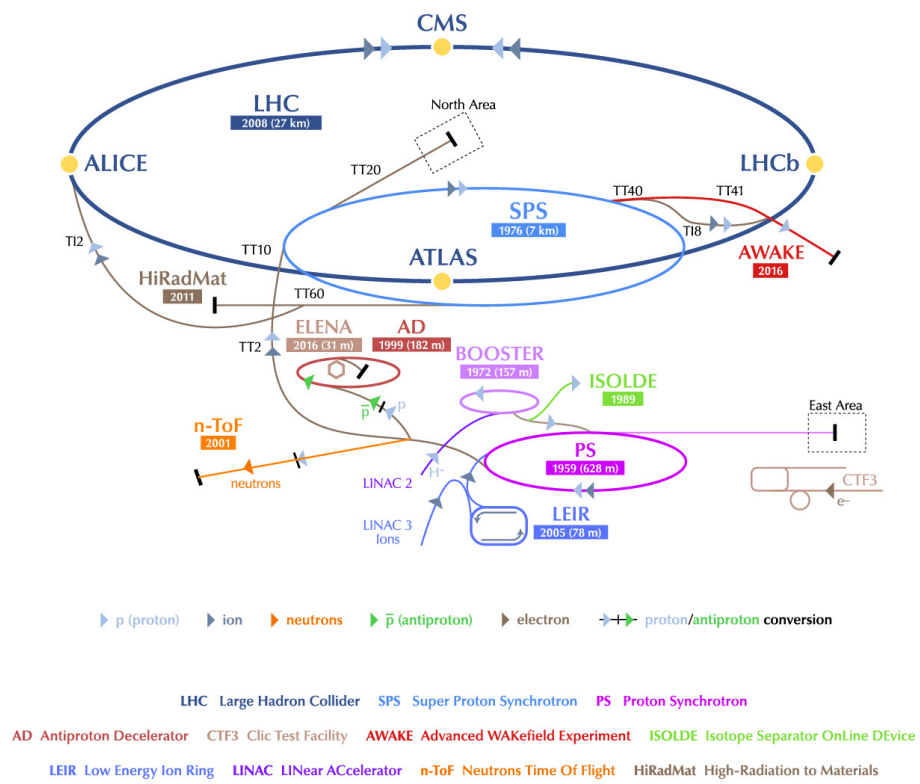


Figure 2.1: The schematics of the accelerators and beamlines in CERN [22].



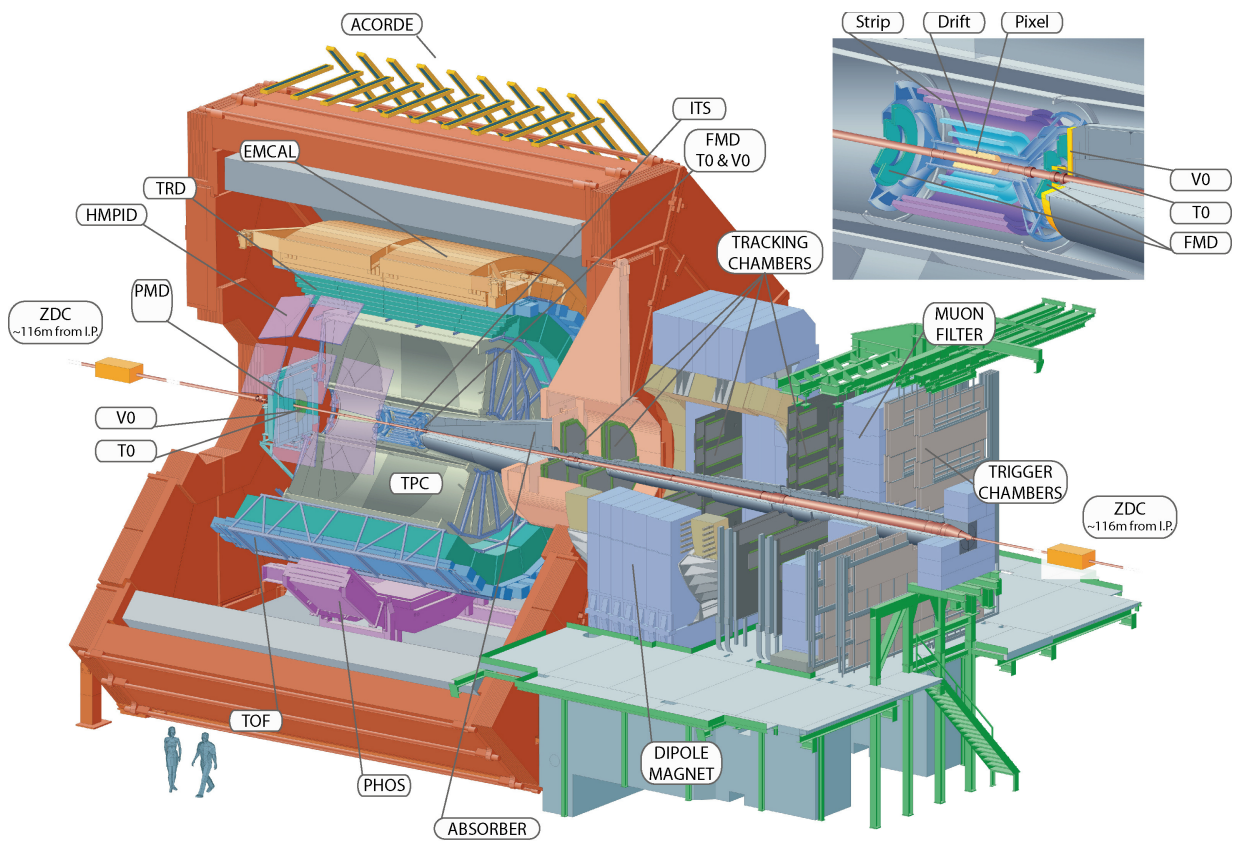


Figure 2.2: The schematic depiction of the ALICE experiment at the LHC. The detail of the ITS and the forward detectors is seen in the upper right corner. The L3 magnet is coloured red.

### 2.2.1 Inner Tracking System (ITS)

The ITS [23] consists of six layers of silicon detectors. **Silicon Pixel Detectors** are the two innermost layers. The middle two layers consist of **Silicon Drift Detectors**. The two outermost layers are **Silicon Strip Detectors**. Each of the six layers is centered around the vertex diamond and the beam goes through the axis. The radii of the layers are 3.9, 7.6, 15.0, 23.9, 38.0, 43.0 cm. The material budget of the ITS is about 8 % of the radiation length. The ITS covers the pseudorapidity range of  $\eta \in (-0.9, 0.9)$ . The first layer has a more extended pseudorapidity coverage  $|\eta| < 1.98$  to provide, together with the Forward Multiplicity Detectors (FMD), continuous coverage for the measurement of charged particles multiplicity. The ITS is illustrated at the top right corner of Figure 2.2.

Its purpose is to determine the position of the primary and secondary vertices in a collision and to aid tracking and particle identification.

### 2.2.2 Time Projection Chamber (TPC)

The TPC [24], seen in Figure 2.2 in grey around the ITS, is the main detector in ALICE that provides tracking and PID (particle identification based on  $dE/dx$ ). It is a cylinder with an inner radius of 85 cm, an outer radius of 250 cm and a length of 500 cm. It is filled with the mixture of He/CO<sub>2</sub> which has to be kept at a constant temperature with fluctuations smaller than 0.1 K in order to minimize the dependence of multiple scattering in the gas on temperature. The electromagnetic field in the TPC is generated by a central cathode and end plate cap anodes with the potential gradient 400 V/cm with collinear electric and magnetic fields. A particle propagating through the chamber ionizes the gas which produces electron-ion pairs. Ions drift to the central electrodes and electrons drift in the electromagnetic field to the multi-wire proportional chambers at the end caps of the TPC. These electrons provide the  $x$  and  $y$  coordinates in the transverse plane to the beam axis of the vertex where the ionization occurred. The  $z$  coordinate is obtained from the drift time.

### 2.2.3 V0

The V0 [25] detector consists of two rings of plastic scintillators V0A at forward,  $2.8 < \eta < 5.1$ , and V0C at backward,  $-3.7 < \eta < -1.7$  pseudorapidities. V0A is 340 cm from the centre of the detector and V0C 90 cm. This asymmetry is caused by an absorber in the muon arm. Both disks are segmented into 32 individual scintillators placed in 4 concentric rings. The V0 detector is used for triggering and measurement of centrality and reaction plane angle. Its location can be seen in Figure 2.3.

### 2.2.4 Computational infrastructure

The analysis has been carried out in the *Aliroot* software. It is built on the *C++* framework called ROOT. The computation has been carried out on the CERN grid.

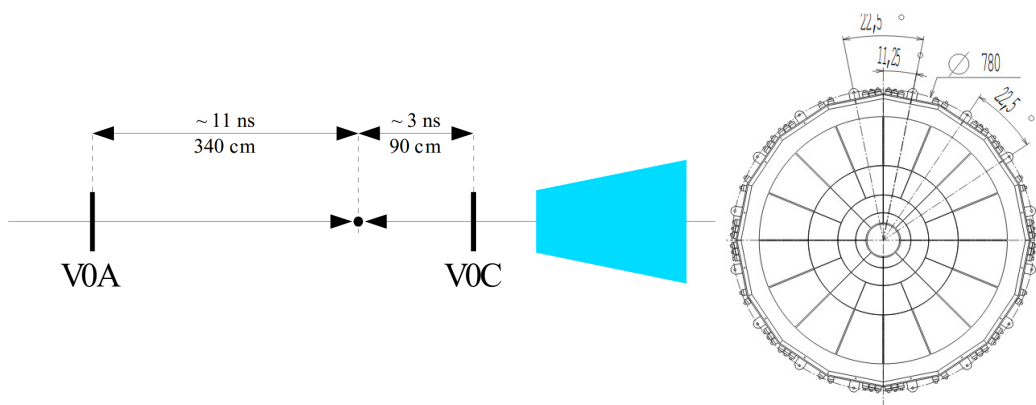


Figure 2.3: **Left:** The location of the V0A and V0C detector. **Right:** The shape of the V0 detectors. Taken from [25].



## Chapter 3

# Analysis of $p_T$ spectra of inclusive charged jets in $p + p$ collisions at $\sqrt{s} = 13$ TeV

The goal of this thesis is to analyse inclusive  $p_T$  spectra of charged anti- $k_T$  jets produced in  $p + p$  collisions at  $\sqrt{s} = 13$  TeV in ALICE. This chapter specifies event selection, track selection criteria and jet reconstruction.

The analysis is based on data from 2016 (period *2016l*).  $p + p$  data from 2015 (period *2015f*) has initially been considered however it did not pass the criteria for uniformity in detector efficiency as shown later. The analysed run numbers from *2015f* and *2016l* are quoted in Table 3.1.

<i>2015f</i> :	226085, 226170, 226175, 226176, 226177, 226183, 226208, 226210, 226212, 226217, 226220, 226225, 226444, 226445, 226452, 226466, 226468, 226472, 226476, 226483, 226495, 226500, 226532, 226543, 226551, 226554, 226569, 226573, 226591, 226593, 226596, 226600, 226602, 226603, 226605, 226606
<i>2016l</i> :	259389, 259394, 259395, 259396, 259473, 259477, 259649, 259650, 259668, 259697, 259700, 259703, 259704, 259705, 259711, 259713, 259747, 259748, 259750, 259751, 259752, 259756, 259781, 259788, 259789, 259822, 259841, 259842, 259860, 259866, 259867, 259868, 259888, 260010, 260011, 260014

Table 3.1: Analysed run numbers.

### 3.1 Event selection

The *V0AND* trigger has been used to trigger events. This trigger requires a time coincidence in the opposite *V0A* and *V0C* scintillation detectors to trigger an event.

The quality of the selected primary interaction vertex and its position is constrained by means of several criteria listed in the *Aliroot* function *AliAnalysisUtils::IsVertexSelected2013pA()*. Events that pass the vertex cut must satisfy these conditions

1. The primary vertex must be reconstructed with at least one contributor

	Before cuts	After pile up cut	After vertex cut
2015f	$7.96 \times 10^7$	$6.66 \times 10^7$	$6.66 \times 10^7$
2016l	$4.43 \times 10^7$	$4.02 \times 10^7$	$4.02 \times 10^7$

Table 3.2: The number of events that survived the different cut stages.

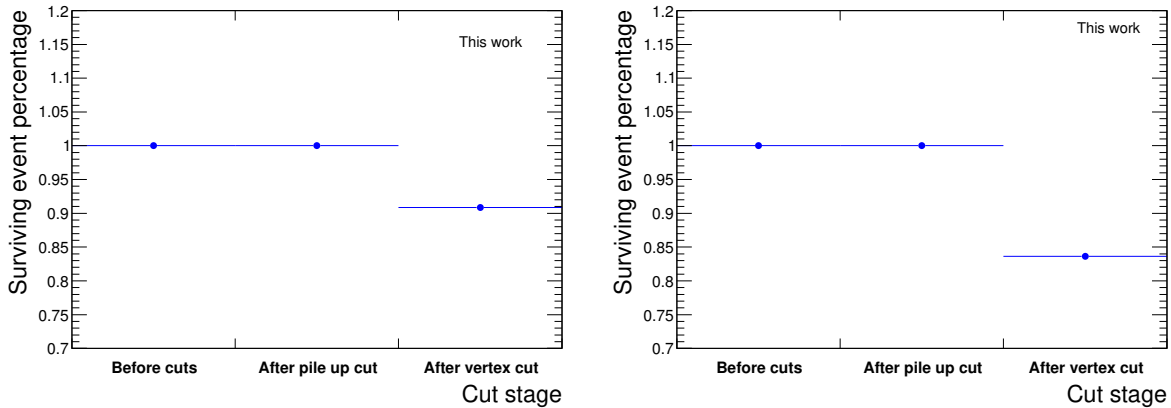


Figure 3.1: Events that survived the different cut stages. **Left:** 2016l. **Right:** 2015f

2. The primary vertex must be reconstructed using data from the SPD
3. The deviation of the  $z$  coordinate of the vertex  $z_{\text{vert}}$  must be within 10 cm from the centre of the detector
4. If the vertex was reconstructed with a fallback vertex finder the errors have to be small

At high collision rates it is possible that several collisions occur in the same bunch crossing and overlap in the detector. This is known as *pile up* and needs to be corrected in the analysis. The pile up cut is carried out by the *Aliroot* function `AliAnalysisUtils::IsPileUpEvent()`. The numbers of events that survived the pileup and vertex cuts are shown in Table 3.2 and Figure 3.1.

Figure 3.1 shows the fraction of the events that survived the pilup and vertex cuts. Figure 3.2 shows the distribution of the  $z$ -vertex for events before the vertex cut is applied.

### 3.2 Track selection

In order to ensure uniform azimuthal track distribution, which is essential for the analysis of jets, so-called *hybrid tracks* are used [26]. Hybrid tracks consist of higher quality *global tracks* and lower quality *complementary tracks*. The conditions that global and complementary tracks have to satisfy are

- Require TPC refit. The ALICE track reconstruction can be described as follows. Tracks are first reconstructed using TPC points extrapolated inwards to the SPD. Then an outward track reconstruction is done starting from SPD. The third step is the TPC refit which refits the tracks in the TPC.
- Crossed row cuts in the TPC. The end caps of the TPC consist of 159 pad rows. Only tracks which have at least 70 rows crossed are accepted.

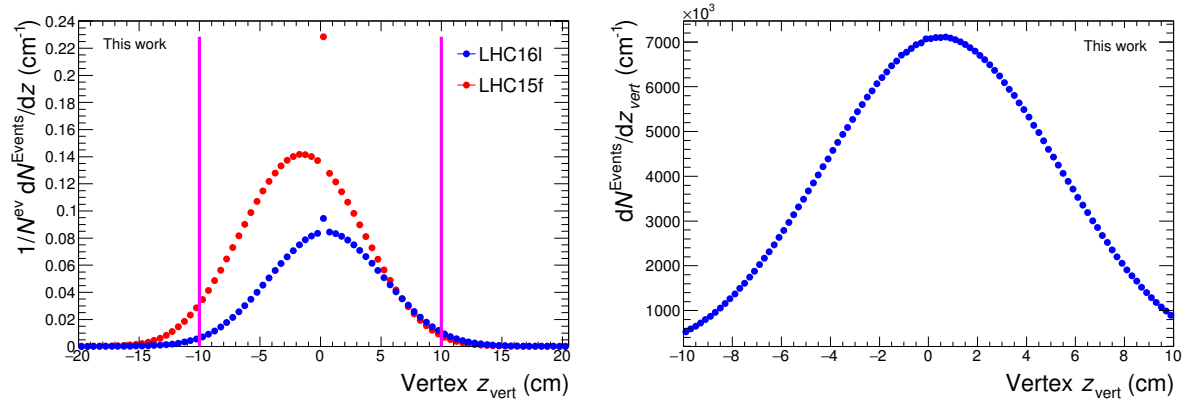


Figure 3.2: **Left:** The  $z$ -distribution of the primary vertex before event selection cuts. Magenta lines indicate the position of the vertex cut. The spike at  $z_{\text{vert}} = 0$  comes from events with no reconstructed vertices. Events from *2016l* are marked by blue circles and events from *2015f* by red circles. **Right:** The  $z$ -distribution of the primary vertex after event selection cuts for the *2016l* period.

- The maximum fraction of shared TPC clusters should be 40%.
- $\chi^2$  on each of reconstructed TPC and ITS clusters should be at most 4.
- $\chi^2 < 36$  for global constrained tracks.
- Tracks that have a kink in the TPC are rejected.
- Transverse momentum cut:  $p_{\text{T}}^{\text{track}} > 150 \text{ MeV}/c$ . This is to ensure sufficient reconstruction efficiency.
- Pseudorapidity cut:  $|\eta^{\text{track}}| < 0.9$ . This is to ensure a uniform acceptance and efficiency of reconstruction.
- For global tracks: Demand ITS refit and at least one hit in SPD.
- For the complementary tracks: No ITS refit or SPD hits are required.

The composition of tracks can be seen in Figure 3.3. The tracks in the period *2015f* are composed of 91.75 % global tracks and in the period *2016l* global tracks constitute 94.89 % of the total.

The efficiency  $\mathcal{E}$  of the reconstruction of tracks can be estimated using Monte Carlo simulations. This is done by introducing the notion of *primary* and *fake* tracks. Physical primary tracks correspond to particles from electromagnetic or strong decays [27]. This is due to the fact that these particles have very short lifetimes and therefore do not propagate far from the primary vertex before decaying. Fake primary tracks are tracks that originated in a weak decay or are reconstructed from segments of different particles.

The cuts in the analysis are tuned to preferentially suppress the number of fake tracks and keep primary tracks. The probability that a primary track will pass the cuts is determined by the reconstruction efficiency which is estimated as

$$\mathcal{E} = \frac{N_{\text{rec}}(p_{\text{T}}^{\text{part}})}{N_{\text{prim}}(p_{\text{T}}^{\text{part}})}, \quad (3.1)$$

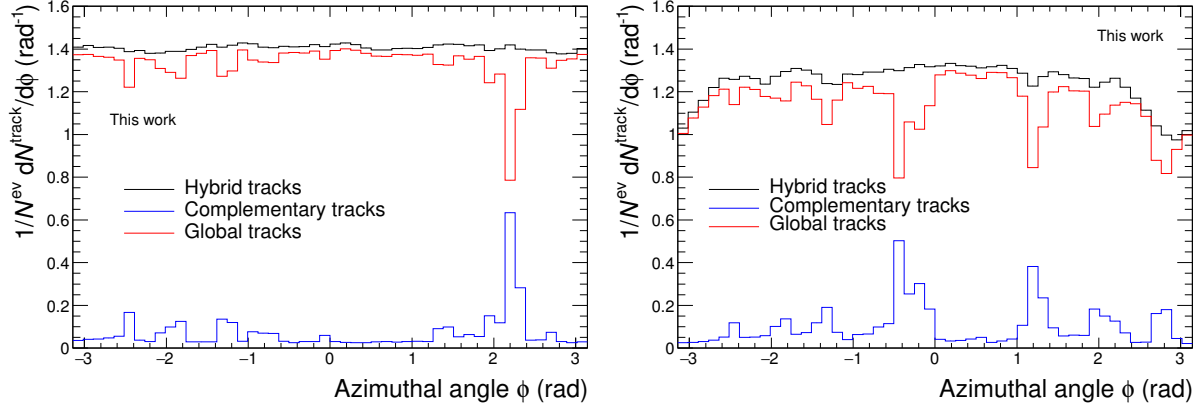


Figure 3.3: Hybrid track composition normalized per the number of events and bin width. **Left:** 2016l. **Right:** 2015f

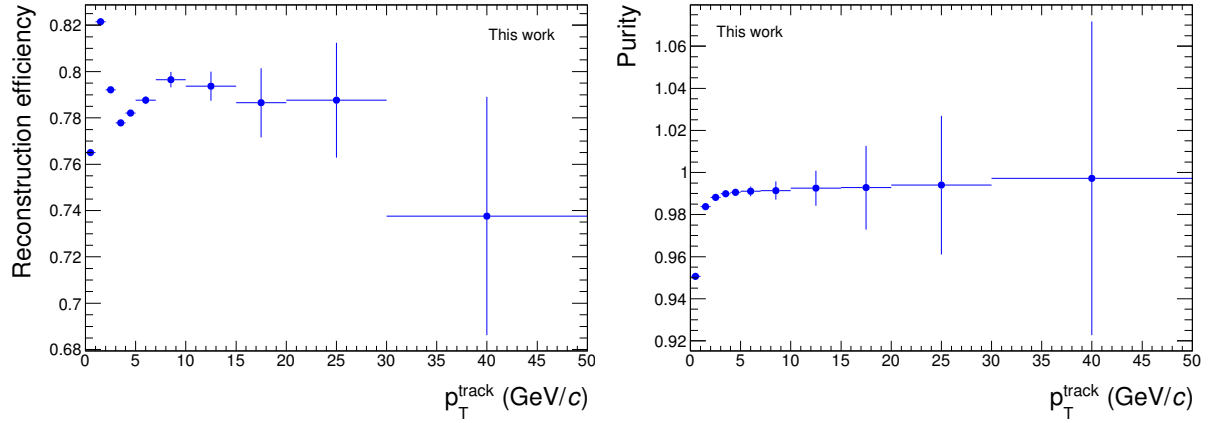


Figure 3.4: **Left:** The efficiency of track reconstruction for the period 2016l based on the Monte Carlo simulation 2016j2a2. **Right:** The purity of reconstructed tracks in 2016l based on the Monte Carlo simulation 2016j2a2.

where  $N_{\text{rec}}$  is the number of tracks reconstructed by the detector and  $N_{\text{prim}}$  is the number of generated tracks and  $p_T^{\text{part}}$  is the transverse momentum of particles from the event generator i.e. the  $p_T$  not affected by the detector. The purity  $\mathcal{P}$  of the reconstructed tracks is obtained as

$$\mathcal{P} = \frac{N_{\text{rec}}(p_T^{\text{part}})}{N_{\text{rec}}(p_T^{\text{part}}) + N_{\text{fake}}(p_T^{\text{det}})}, \quad (3.2)$$

where  $N_{\text{fake}}$  is the number of fake tracks reconstructed by the detector and  $p_T^{\text{det}}$  is the  $p_T$  assigned to the particle by the reconstruction. The reconstruction efficiency and purity of tracks estimated from PYTHIA 6 Perugia 11 the Monte Carlo simulation 2016j2a2 for the period 2016l is seen in Figure 3.4. The efficiency of track reconstruction is approximately 80 % for particles with  $p_T > 5$  GeV/c. The reconstruction efficiency for particles below 5 GeV is affected by the bending of tracks in the magnetic field which can then pass through inefficient regions in ALICE (e.g. sector borders in TPC). The purity of tracks with  $p_T > 1$  GeV/c is better than 98 %.



### 3.3 Jet selection

Jets are reconstructed from charged tracks using the  $k_T$  and anti- $k_T$  algorithms with  $R = 0.4$ . *FastJet-v3.1.3* [15] has been used for the clusterisation of jets. In order to eliminate jets that have been effected by the loss of particles that fall outside the detector acceptance further cut on the jet pseudorapidity are applied. Such jets would have a naturally reduced  $p_T$ . The pseudorapidity of jets has to satisfy  $|\eta^{\text{jet}}| < 0.9 - R$  where  $R$  is the jet resolution roughly measuring the radius of the jet cone. Tracks are assumed to correspond to massless particles and their 4-momenta. The 4-momenta were added using the recombination  $E$ -scheme [15]. The used ghost area is 0.01. The  $p_T$  of jets is corrected for the underlying event using approaches described in section 1.8.

### 3.4 Data quality assurance

Before the analysis of  $p_T$  spectra can be carried out it is necessary to check that the conditions for data taking in each run were similar. The stability of tracking can be conveniently checked by inspecting the mean track multiplicity on a run-by-run basis together with the corresponding pseudorapidity and azimuthal angle distributions of reconstructed tracks.

#### 3.4.1 2015f

The average track multiplicity of the *2015f* dataset is seen in Figure 3.5. Runs with zero mean track multiplicity have to be excluded from further analysis. Further abnormalities are marked by red arrows and an ellipse in Figure 3.5. A closer examination of these runs reveals problems with the detectors.

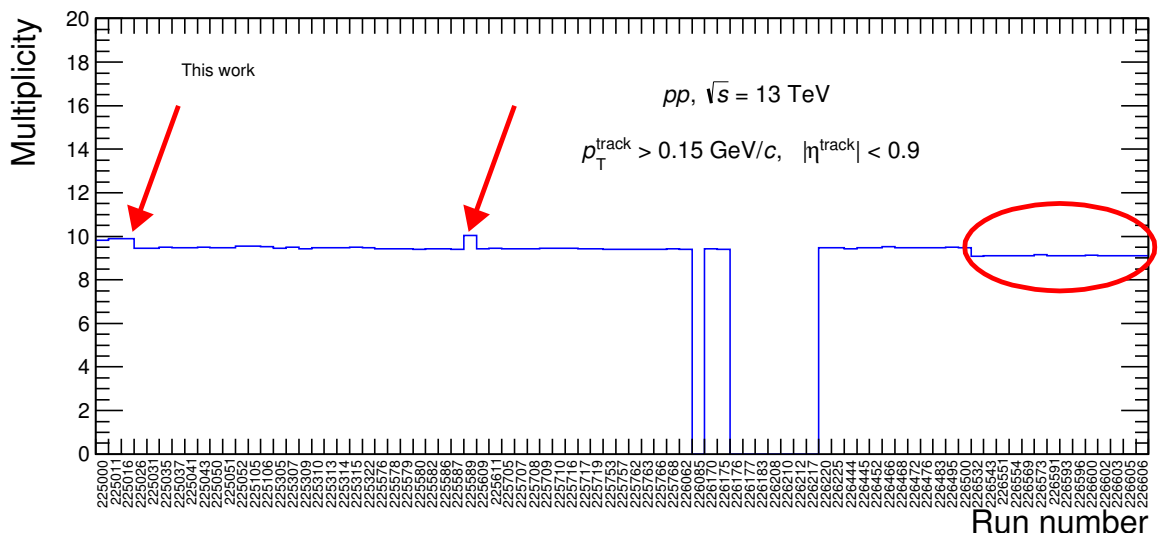


Figure 3.5: Average track multiplicity versus the run number in the whole *2015f* period.

Figure 3.6 shows a comparison of per event normalized pseudorapidity distributions of charged tracks with  $p_T > 150 \text{ MeV}/c$  of produced tracks in three runs that are representatives of each of the three regions. The set *225011* is a sample from the higher multiplicity

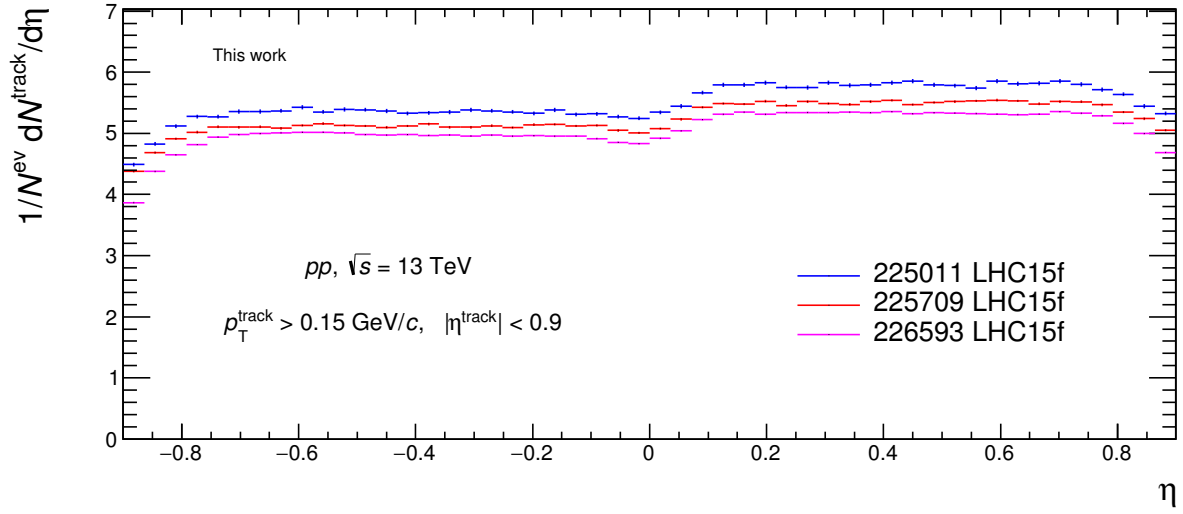


Figure 3.6: Comparison of the pseudorapidity distributions of tracks in runs representing three different regions from the *2015f* period. Distributions are normalized per event and bin width.

region, the set *225709* is a sample set from the average multiplicity region and *226593* is a sample from the lower multiplicity region. Figure 3.6 exhibits an asymmetry in  $\eta$ . This asymmetry is not expected from physics since the collision system is symmetric. The azimuthal distribution, seen in Figure 3.7, further confirms strong irregularities in the detector efficiency, namely a large inefficiency region at  $\phi = \pi$ . In an ideal case, this distribution is supposed to be uniform because the collision system is symmetric. A jet analysis requires a uniform detector efficiency across the angular acceptance. If this condition had not been met the jet algorithm would preferentially create jets in the regions with higher reconstruction efficiency. The whole *2015f* dataset has therefore been excluded from all further analysis.

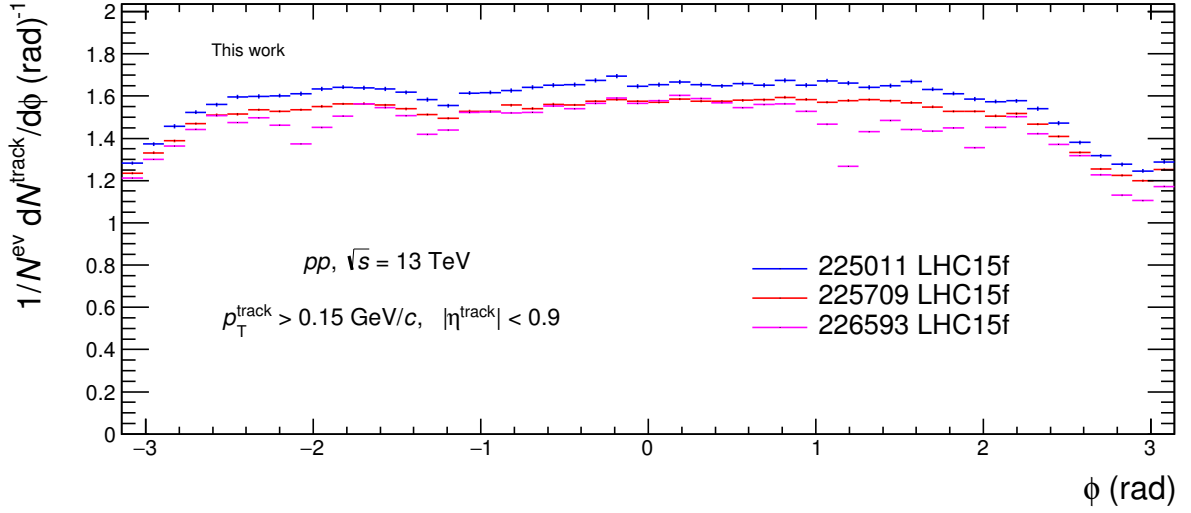


Figure 3.7: Comparison of the azimuthal distributions of tracks in runs representing three different regions from the *2015f* period. Distributions are normalized per event and bin width.

### 3.4.2 2016l

The average charged track multiplicity is plotted in Figure 3.8.

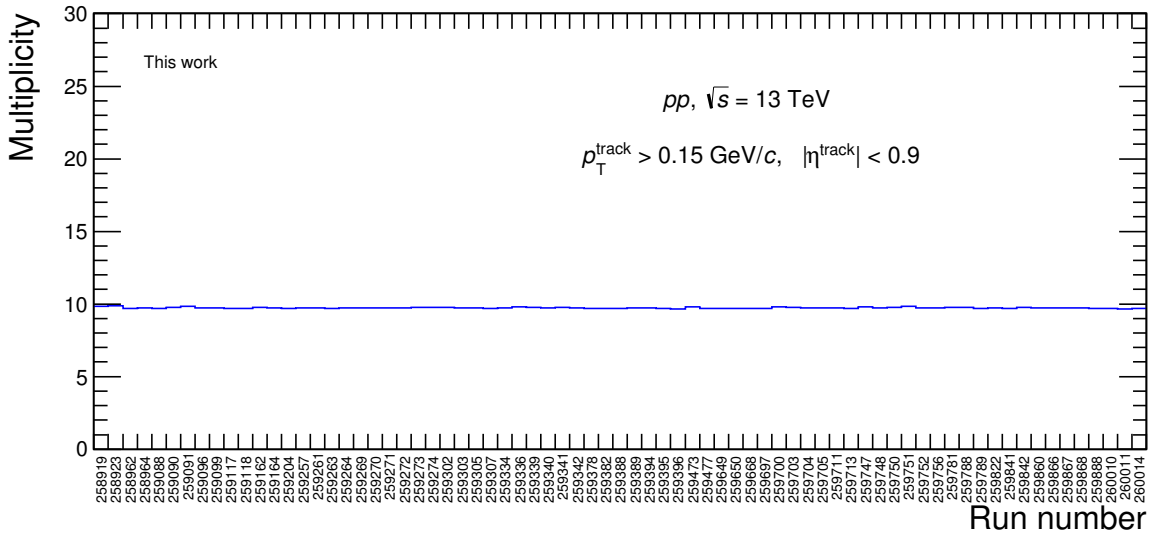


Figure 3.8: Average track multiplicity versus the run number in the whole *2016l* period.

Pseudorapidity and azimuthal distributions show no significant problems. An example comparison of two runs from *2016l* period is shown in Figures 3.9 and 3.10. The distributions are symmetric as expected. The dip in the pseudorapidity distribution at  $\eta = 0$  is caused by the central electrode of the TPC.

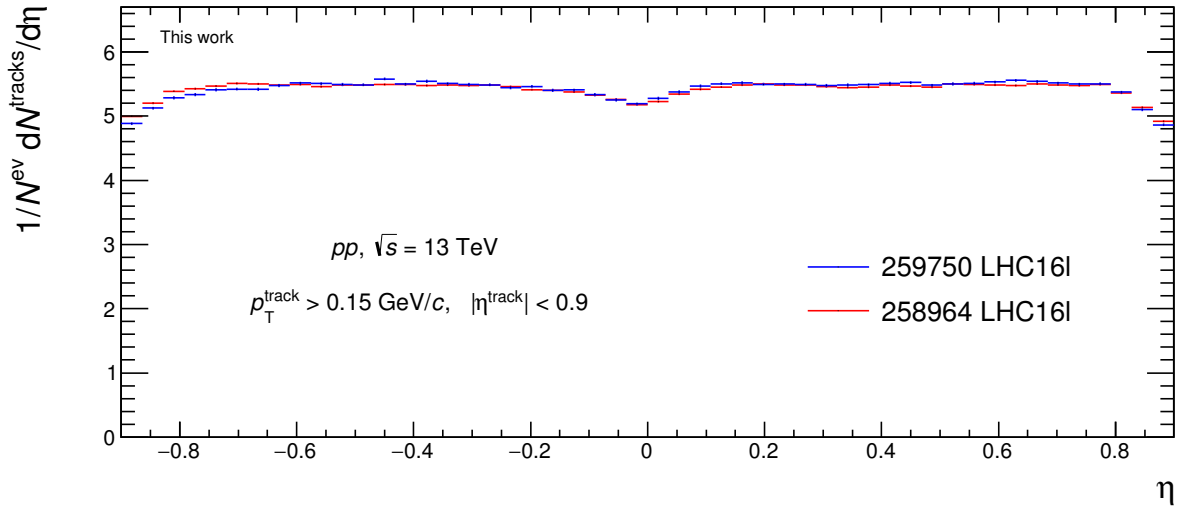


Figure 3.9: An example of the comparison of charged track pseudorapidity distributions of two datasets from the *2016l* period. Distributions are normalized per event and bin width.

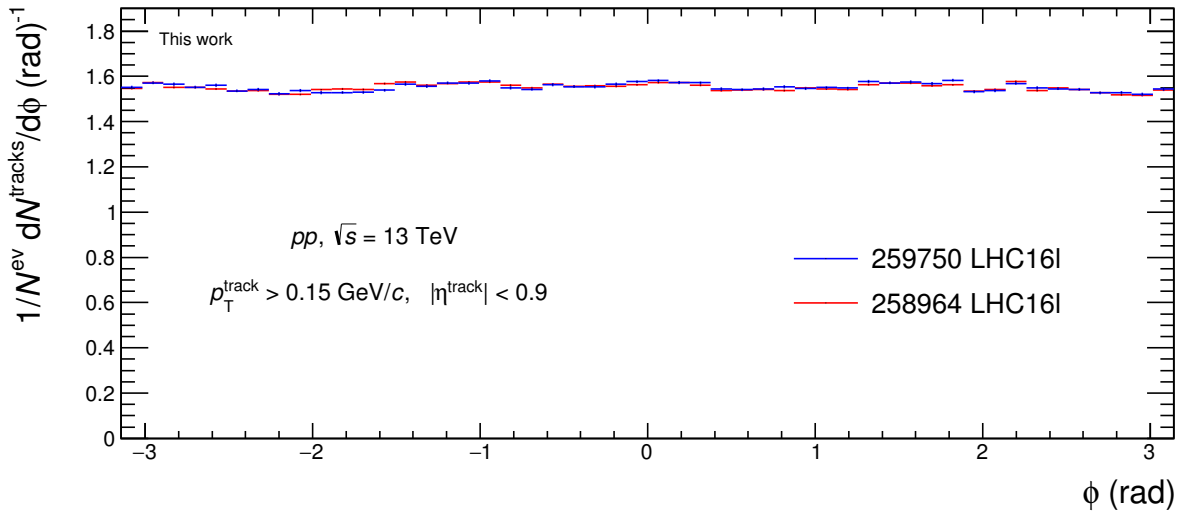


Figure 3.10: An example of the comparison of charged track azimuthal distributions of two datasets from the *2016l* period. Distributions are normalized per event and bin width.

The  $\eta$  distributions are falling at high pseudorapidities due to fewer cross rows of the TPC being crossed. None of the analysed runs exhibits a significant deviation from the average and all of them will be used to analyse  $p_T$  spectra of jets.

## Chapter 4

# Analysis of simulations

Simulations are used to correct the raw data for instrumental effects and to compare the corrected measurements to expectations from an event generator. Simulated p + p collisions at  $\sqrt{s} = 13$  TeV events were generated using PYTHIA 6 [11] with the Perugia 11 tune. The generated PYTHIA events were processed with a detailed GEANT4 model of the ALICE detector and a model of the detector response which reflected the experimental situation for the *2016l* period. Subsequently these data were analysed as real data.

### 4.0.1 Simulated events anchored to runs from *2016l*.

The simulated Perugia 11 events anchored to runs from *2016l* in the Monte Carlo data set *2016j2a2* were used. The *2016j2a2* simulation contains  $4.08 \times 10^7$  simulated events of which  $3.80 \times 10^7$  have passed the event selection. The average track multiplicity is shown in Figure 4.1.

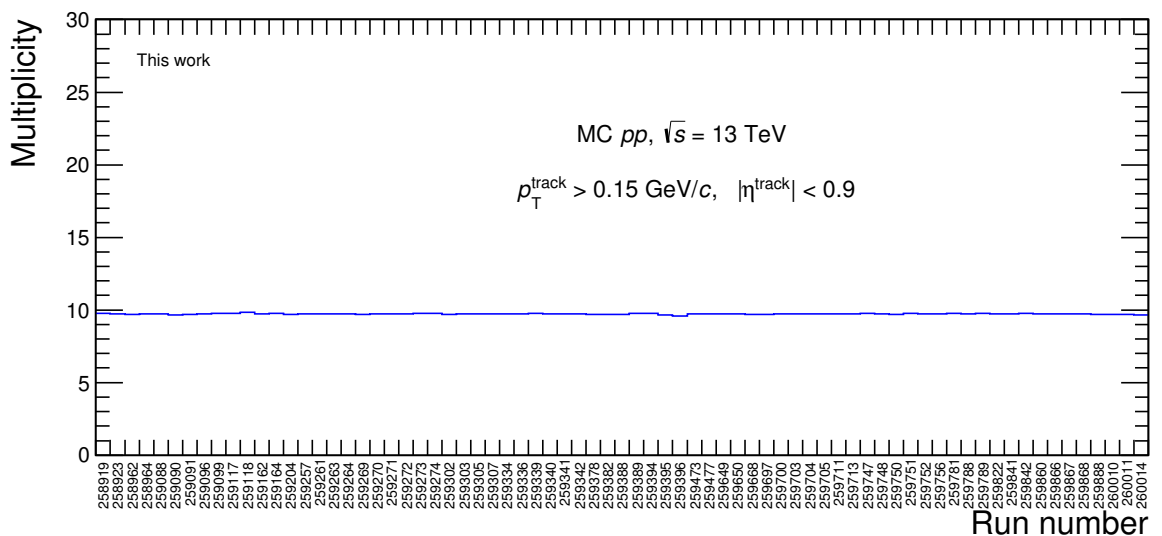


Figure 4.1: Average track multiplicity in the PYTHIA detector level simulation corresponding to the period *2016l* (MC data set *2016j2a2*).

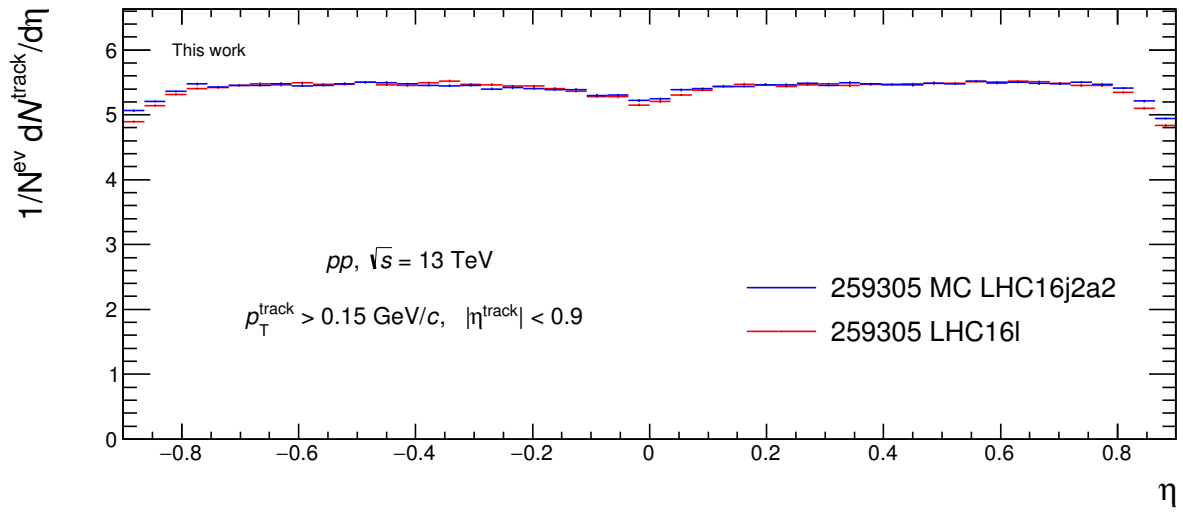


Figure 4.2: Pseudorapidity distributions of tracks with  $p_T > 150$  MeV/ $c$  from the Monte Carlo PYTHIA 6 Perugia 11 simulation *2016j2a2* anchored to *2016l*. Distributions are normalized per event and bin width. The corresponding run numbers are quoted in the legend.

The comparison of pseudorapidity and azimuthal angle distributions of the Monte Carlo PYTHIA 6 Perugia 11 simulation *2016j2a2* anchored to *2016l* is shown in Figures 4.2 and 4.4 for  $p_T > 150$  MeV/ $c$  and for tracks with  $p_T > 3$  GeV/ $c$  in Figures 4.3 and 4.5.

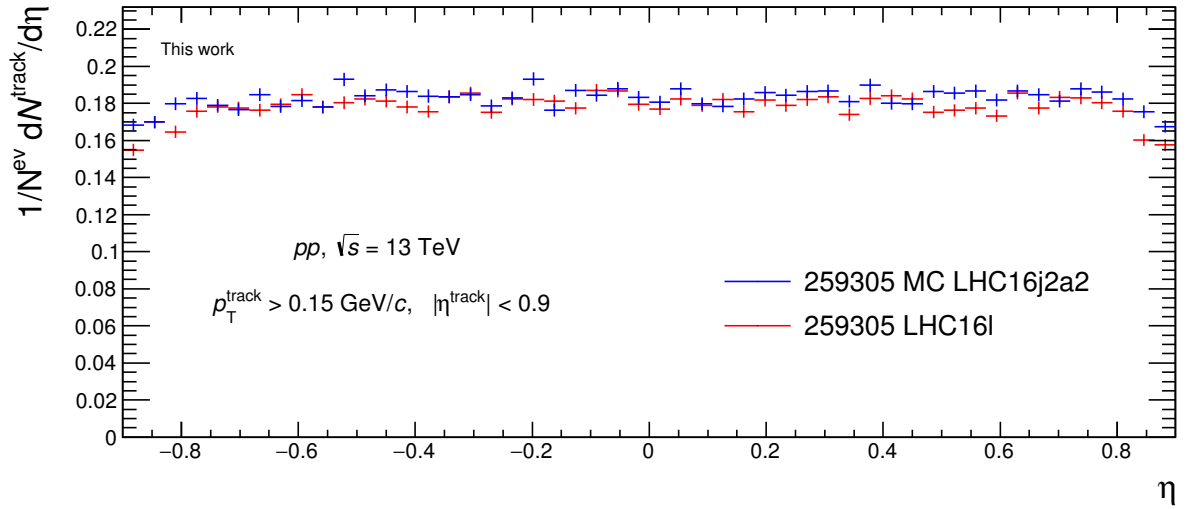


Figure 4.3: Pseudorapidity distributions of tracks with  $p_T > 3 \text{ GeV}/c$  from the Monte Carlo PYTHIA 6 Perugia 11 simulation *2016j2a2* anchored to *2016l*. Distributions are normalized per event and bin width. The corresponding run numbers are quoted in the legend.

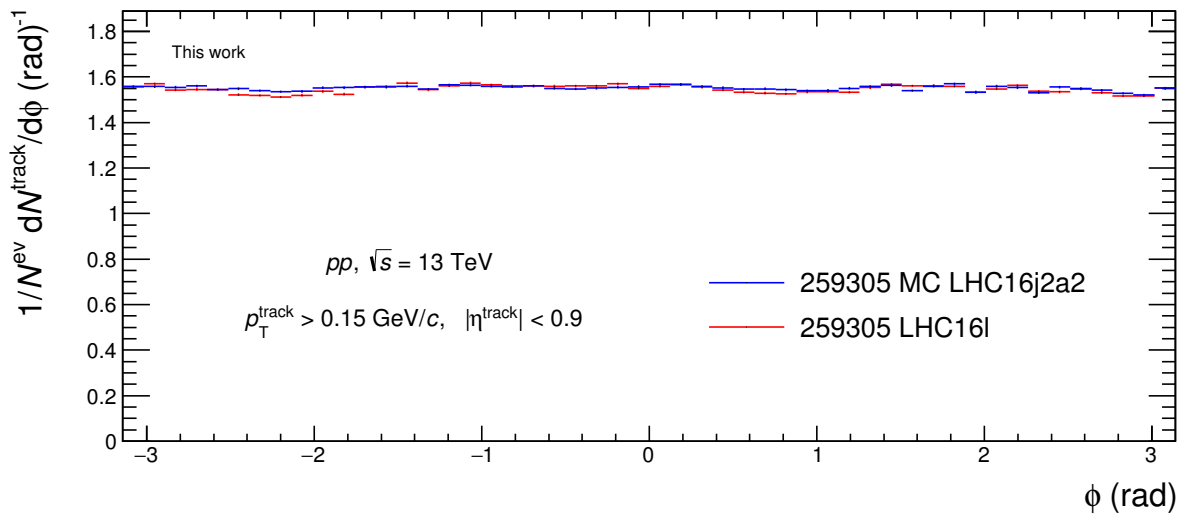


Figure 4.4: A comparison of azimuthal angle distributions of tracks with  $p_T > 150 \text{ MeV}/c$  of corresponding runs from *2016l* and *2016j2a2*. Distributions are normalized per event and bin width.

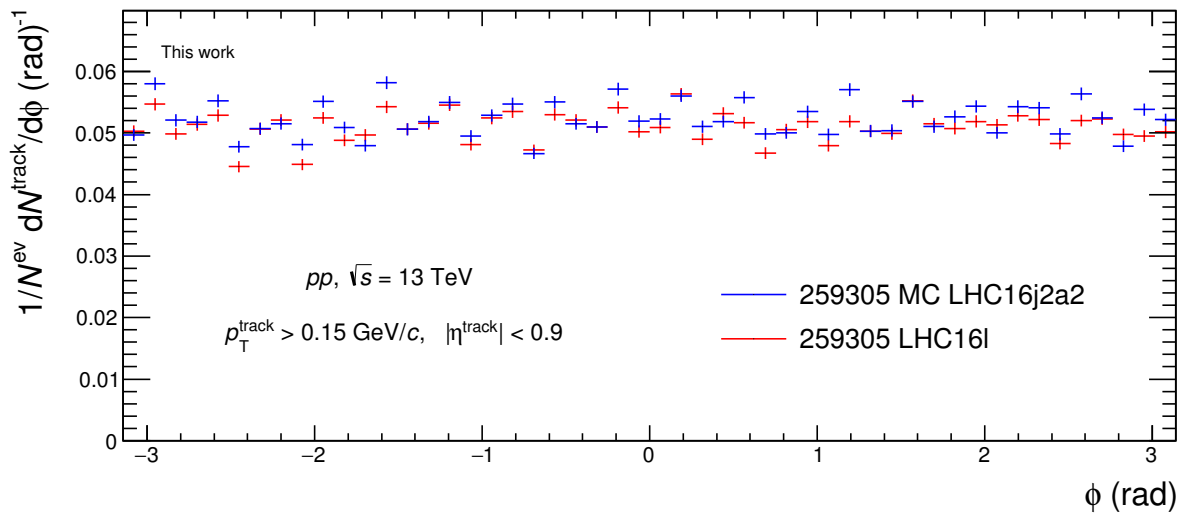


Figure 4.5: A comparison of azimuthal angle distributions of tracks with  $p_T > 3 \text{ GeV}/c$  of corresponding runs from 2016l and 2016j2a2. Distributions are normalized per event and bin width.



## Chapter 5

# Raw jet $p_T$ spectra

In this chapter, inclusive, charged, anti- $k_T$ ,  $R = 0.4$  jet  $p_T$  spectra from p + p collisions at  $\sqrt{s} = 13$  TeV obtained from the period 2016/ are shown. The raw, unnormalised jet  $p_T$  spectrum is seen in Figure 5.1. This spectrum needs to be corrected for detector effects and background

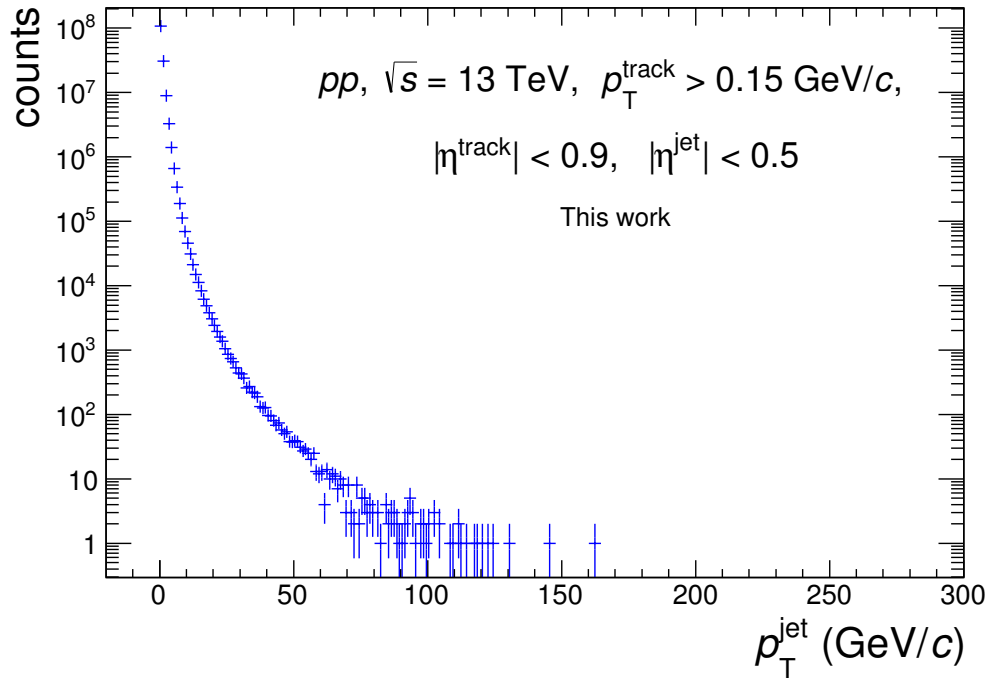


Figure 5.1: The unnormalised raw jet  $p_T$  spectrum from the period 2016/ with the bin width of 1 GeV/c. Uncorrected for background

fluctuations. The corresponding unfolding procedure is more stable when the statistics in bins is large enough (ALICE analyses use at least 10 counts per bin). Therefore the spectrum is rebinned and a larger bin width in sparsely populated regions is used. The chosen binning for the raw spectrum is

$$p_T^{\text{bins}} = \{3, 4, 5, 6, 8, 10, 12, 16, 20, 25, 30, 40, 60, 90\} \text{ (GeV/c)}. \quad (5.1)$$

The spectrum after rebinning is seen in Figure 5.2.

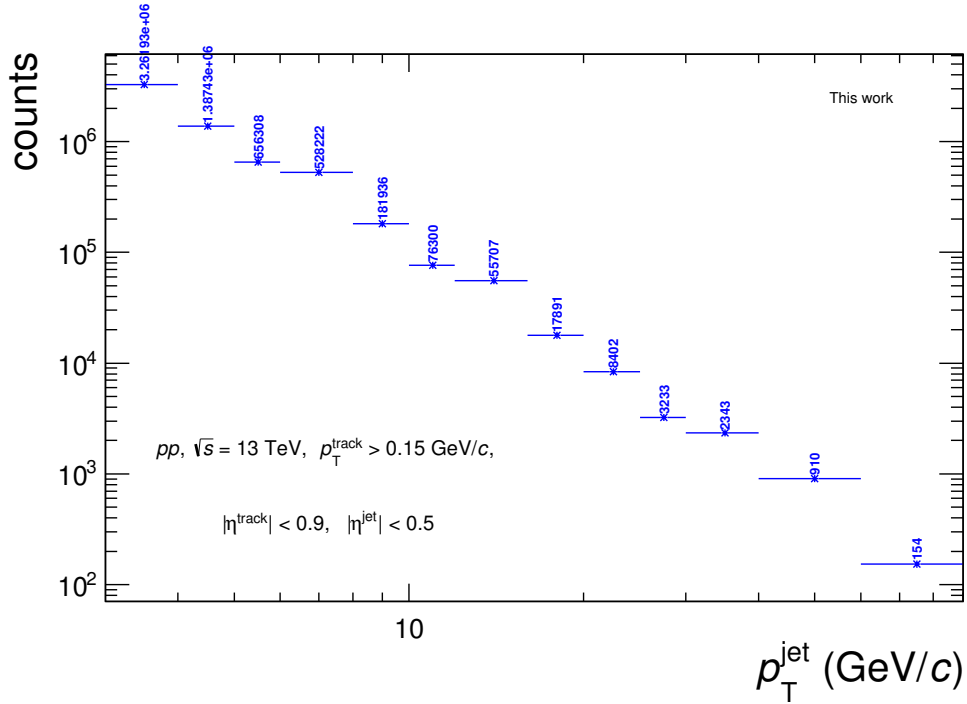


Figure 5.2: The unnormalised raw jet  $p_T$  spectrum from the period 2016/. The spectrum has been rebinned according to (5.1). The numbers above each bin give the number of counts.

In order to compare the raw spectrum to the Monte Carlo spectrum, the spectra are normalised per the number of events and the bin width. The comparison is depicted in Figure 5.3.

The uncorrected jet  $p_T$  spectrum as well as the corrected spectra using the standard area based approach and the perpendicular cones approach are shown in Figure 5.4. The background density  $\rho$  as well as the  $p_T$  correction  $A^{\text{jet}} \times \rho$  from the two methods is shown in Figure 5.5.

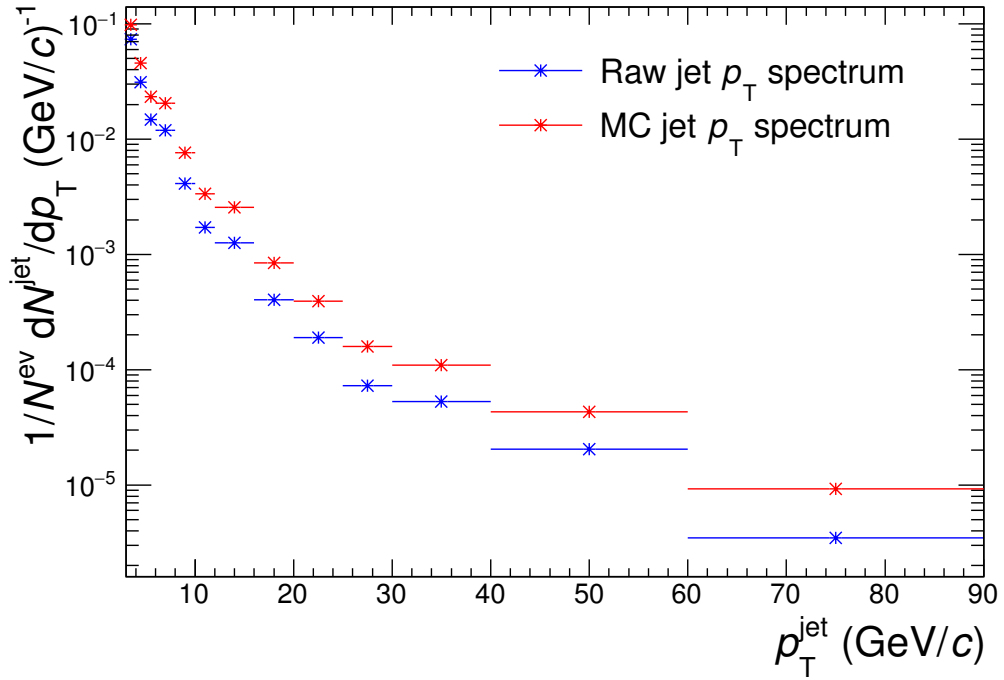


Figure 5.3: The per-event and per-bin-width normalised jet  $p_T$  spectra from the period *2016/* and the PYTHIA 6, Perugia 11 Monte Carlo simulation *2016j2a2*. The spectrum has been rebinned according to (5.1).

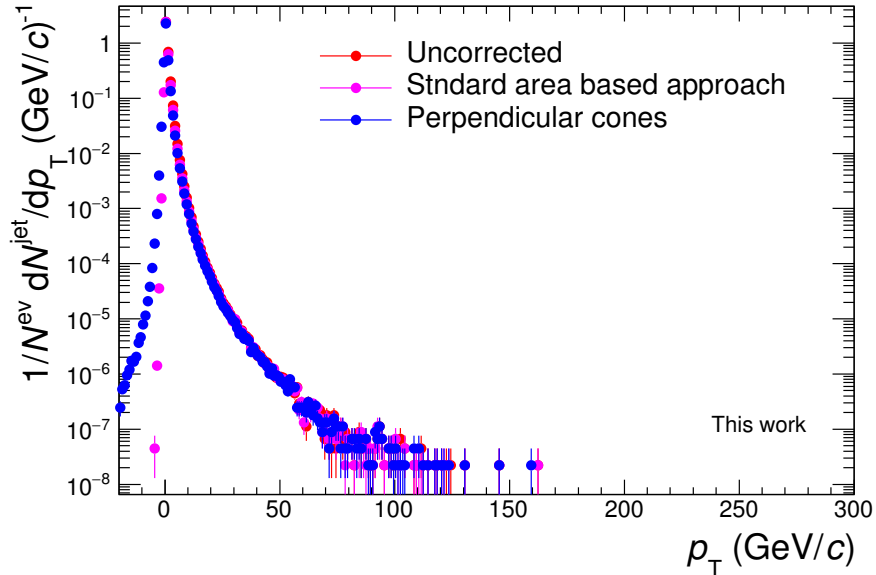


Figure 5.4: The corrected jet spectra of the period in comparison with the uncorrected spectrum. The red histogram corresponds to the uncorrected jet  $p_T$ , the magenta to the standard based area approach correction and the blue to the perpendicular cones correction. All spectra are from the *2016/* period.

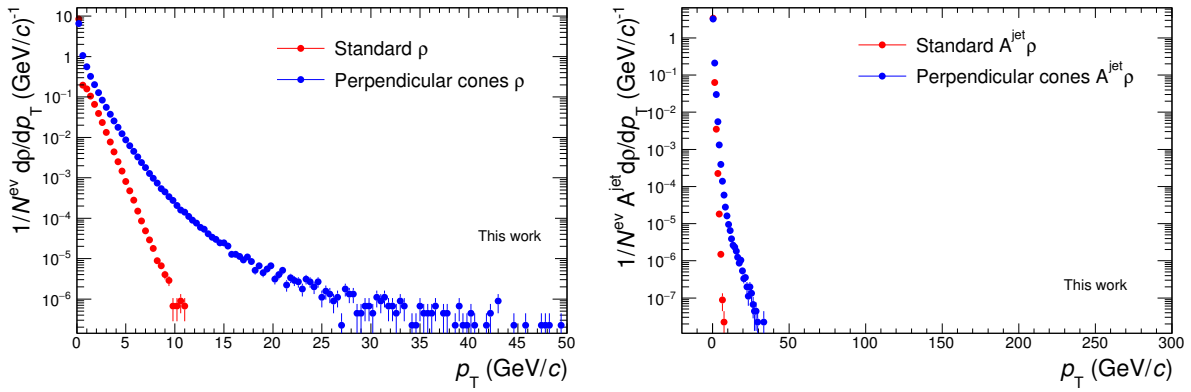


Figure 5.5: **Left:** The underlying event density  $\rho$  as calculated with the standard area based approach and the perpendicular cones method. **Right:** The  $p_T$  correction  $A^{\text{jet}}\rho$  as calculated with the standard area based approach and the perpendicular cones method. Both quantities are calculated from the *2016l* dataset.

# Chapter 6

## Unfolding

Raw jet  $p_T$  spectra measured by a real detector suffer for the inherent flaws of the detector such as the inefficiency of track reconstruction and track momentum smearing. The measured raw jet spectra need to be corrected for these detector effects. In this analysis, these corrections are carried out by *unfolding* based on the singular value decomposition theorem.

Suppose that the bins of the measured jet  $p_T$  spectrum are represented by the elements of a vector  $\vec{b}$ . A linear relation between the original spectrum  $\vec{x}$  and the reconstructed  $p_T$  spectrum  $\vec{b}$  is assumed. The detector effects are represented by the *response matrix*  $\mathbb{A}$  of the detector. The desired true  $p_T$  distribution of jets  $\vec{x}$  is then obtained by solving the linear system for  $\vec{x}$

$$\vec{b} = \mathbb{A}\vec{x}. \quad (6.1)$$

The response matrix  $\mathbb{A}$  may be singular and therefore simple matrix inversion is insufficient.

### 6.1 Singular Value Decomposition

To invert the matrix  $\mathbb{A}$ , an approach based on the singular value theorem [28] is utilised.

**Theorem 1 (SVD).** *Let  $\mathbb{A} \in \mathbb{R}^{m,n}$  be an arbitrary matrix where  $n, m \in \mathbb{N}$ . Then  $\mathbb{A}$  admits a decomposition of the form*

$$\mathbb{A} = \mathbb{U}\mathbb{S}\mathbb{V}^T, \quad (6.2)$$

where  $\mathbb{U} \in \mathbb{R}^{m,m}$  and  $\mathbb{V} \in \mathbb{R}^{n,n}$  are orthogonal matrices and  $\mathbb{S} = \text{diag}(\mathbb{S}_{11}, \mathbb{S}_{22}, \dots, \mathbb{S}_{rr})$ . The numbers  $\mathbb{S}_{11} \geq \mathbb{S}_{22} \geq \mathbb{S}_{rr} \geq 0$  are called the *singular values* of  $\mathbb{A}$  where  $r = \text{rank}(\mathbb{A})$ .

The decomposition (6.2) can be interpreted as a rotation represented by the orthogonal matrix  $\mathbb{V}^T$  then a scaling by a diagonal matrix  $\mathbb{S}$  and finally another rotation by an orthogonal matrix  $\mathbb{U}$ .

In [28], the problem (6.1) is transformed into minimising the quadratic form

$$(\bar{\mathbb{A}}\vec{y} - \vec{b})(\bar{\mathbb{A}}\vec{y} - \vec{b})^T + \tau (\mathbb{C}\vec{y})^T \mathbb{C}\vec{y}, \quad (6.3)$$

where the vector  $y_i = \frac{x_i}{x_i^{\text{ini}}}$  and the matrix  $\bar{\mathbb{A}}_i = \mathbb{A}_{ij}x_j^{\text{ini}}$  are rescaled by an initial estimate of the solution  $\vec{x}^{\text{ini}}$ —the so-called *prior spectrum*. This scaling is done in order to make the  $\vec{y}$  slowly varying (ideally,  $\vec{y}$  should be flat). The matrix  $\mathbb{C}$  is added in order to regularise the initial problem which may be singular. The final solution is expected to minimally fluctuate around the prior spectrum and therefore the last term in (6.3) represents the measure of oscillations.

If the measure of oscillations is represented as the square of second derivatives of  $\vec{y}$  then  $\mathbb{C}$  is chosen as the matrix of the second differences between subsequent elements of  $\vec{y}$ . The parameter  $\tau$  represents the strength of the regularisation. The matrix  $\mathbb{C}$  can be expressed as

$$\mathbb{C} = \begin{pmatrix} -1 + \varepsilon & 1 & 0 & 0 & \cdots & 0 \\ 1 & -2 + \varepsilon & 1 & 0 & \cdots & 0 \\ 0 & 1 & -2 + \varepsilon & 1 & \cdots & 0 \\ \vdots & \vdots & \vdots & \vdots & \ddots & \vdots \\ 0 & 0 & 0 & 0 & \cdots & -1 + \varepsilon \end{pmatrix}. \quad (6.4)$$

The small increment  $\varepsilon$  is added to the diagonal in order to make  $\mathbb{C}$  invertible. A sensible choice for  $\varepsilon$  is on the order of  $\varepsilon = 10^{-3}$  [28]. The minimisation of (6.3) is searched by the *damped least squares* method from the overdetermined system

$$\begin{pmatrix} \bar{\mathbb{A}}\mathbb{C}^{-1} \\ \sqrt{\tau}\mathbb{I} \end{pmatrix} \mathbb{C}\vec{y} = \begin{pmatrix} \vec{b} \\ \vec{0} \end{pmatrix}. \quad (6.5)$$

The SVD is now applied on the matrix  $\bar{\mathbb{A}}\mathbb{C}^{-1}$

$$\bar{\mathbb{A}}\mathbb{C}^{-1} = \mathbb{U}\mathbb{S}\mathbb{V}^T. \quad (6.6)$$

The regularised solution of (6.1) can be expressed as

$$\vec{y}^\tau = \mathbb{C}^{-1}\mathbb{V}\vec{z}^\tau, \quad (6.7)$$

where

$$z_i^\tau := \frac{d_i \mathbb{S}_{ii}}{\mathbb{S}_{ii}^2 + \tau}, \quad (6.8)$$

and

$$\vec{d} := \mathbb{U}^T \vec{b}. \quad (6.9)$$

The unfolded solution  $x^{\text{true}}$  is the obtained from  $y^\tau$  by rescaling by the initial prior distribution.

According to [28], the cut-off parameter  $\tau$  can be determined by plotting  $\log|d_i|$  versus  $i$  as in Figure 6.1. The cut-off is chosen at the place where statistically significant components of the vector  $\vec{d}$  change to randomly oscillating which is

$$\tau = \mathbb{S}_{kk}^2, \quad (6.10)$$

where  $k$  is the component indicated by the arrow in Figure 6.1 and  $\mathbb{S}_{kk}$  is the  $k$ -th diagonal element of the matrix  $\mathbb{S}$  from SVD. The components of  $d_i$  where statistical fluctuations dominate are random numbers following  $|N(0, 1)|$ , where  $N(0, 1)$  is the normal distribution with mean 0 and standard deviation 1. If  $|d_i|$  vs.  $i$  is plotted, these components fluctuate around the expectation value  $E[|N(0, 1)|] = \sqrt{\frac{2}{\pi}}$ .

## 6.2 Response matrix

The response matrix of the detector was obtained from the simulated Perugia 11 events *2016j2a2* anchored to the period *2016l* and is seen in Figure 6.2. This is a minimum-bias Monte Carlo production which does not have large enough statistics at high  $p_T$ .

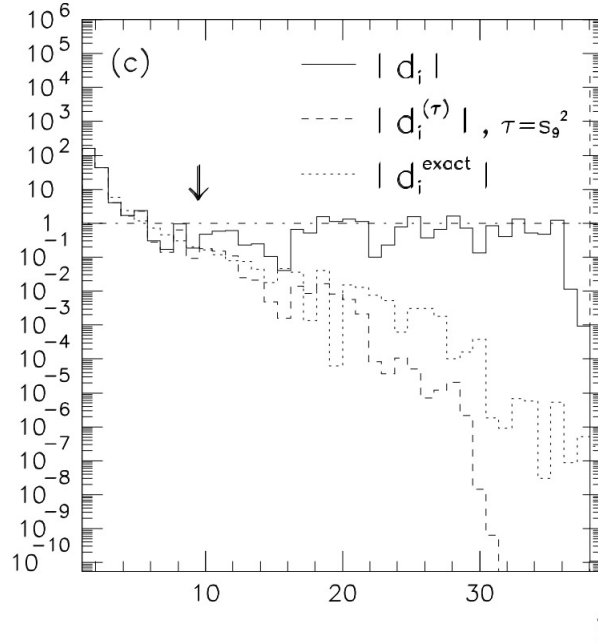


Figure 6.1: Illustration of  $\log|d_i|$  versus  $i$  for choosing the optimal value for  $\tau$ . Taken from [28].

In this case, the response matrix represents the relation between the jet  $p_T$  at the particle level and the corresponding jet  $p_T$  at the detector level. The matching between the corresponding jets at the particle level and at the detector level is done based on their mutual angular distance. The response matrix has been rebinned according to (5.1) in the reconstructed jet  $p_T$  axis and according to

$$p_{T,\text{jet}}^{\text{True}} = \{0, 4, 8, 12, 16, 20, 25, 30, 50, 80, 100\} \text{ (GeV}/c\text{)}, \quad (6.11)$$

in the true jet  $p_T$  axis. The response matrix with this binning is shown in Figure 6.3.

### 6.3 Results

A bin-by-bin correction is the simplest method of jet spectra correction. Each bin of the spectrum is corrected as

$$B = \frac{T^{\text{MC}}}{R^{\text{MC}}} \cdot R^{\text{data}}, \quad (6.12)$$

where  $B$  is the bin content of the corrected spectrum,  $T^{\text{MC}}$  is the bin content of the true spectrum obtained from Monte Carlo,  $R^{\text{MC}}$  is the bincontent of the Monte Carlo reconstructed spectrum and  $R^{\text{data}}$  is the bincontent of the raw spectrum.

The SVD-unfolded and raw jet  $p_T$  spectra from the period 2016I are compared in Figure 6.5. The unfolding has been done with the response matrix seen in Figure 6.3. The prior distribution was generated as minimum-bias, PYTHIA 8 tune 4C, p + p events at  $\sqrt{s} = 13$  TeV and is shown in Figure 6.4. In order to check the consistency of the unfolding, the unfolded spectrum is convoluted with the response matrix. This *folded* spectrum is then compared with the raw spectrum. The comparison of the raw and folded jet  $p_T$  spectra is illustrated in Figure 6.6. In order to determine the optimum cut-off parameter, the ratios of the folded and raw spectra are plotted for several cut-off parameters. This ratio along with the  $d_i$  distribution of the SVD unfolding are shown in Figure 6.7. The regularization parameter  $\tau = 9$  has been chosen.

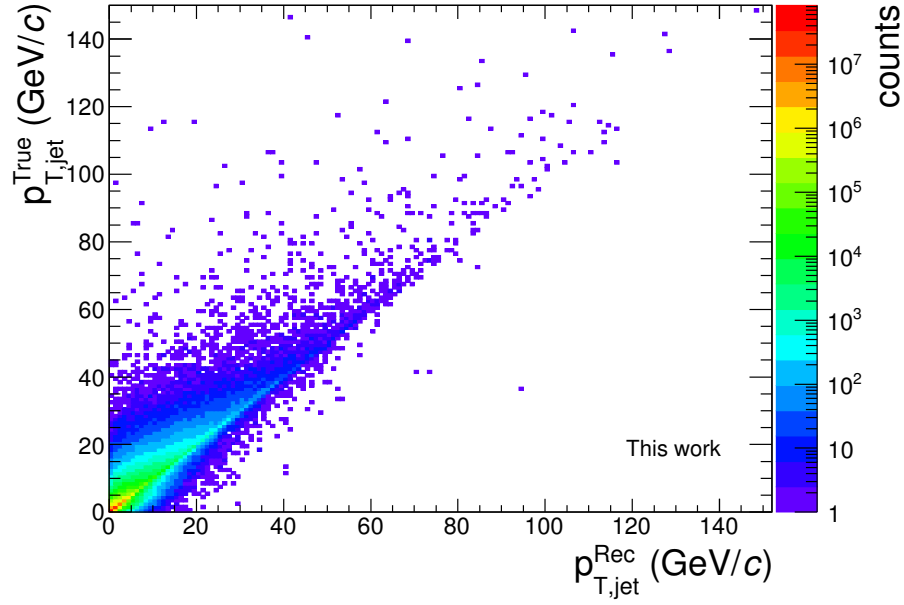


Figure 6.2: The response matrix obtained from the Monte Carlo PYTHIA 6 Perugia 11 simulation *2016j2a2* anchored to *2016l*.

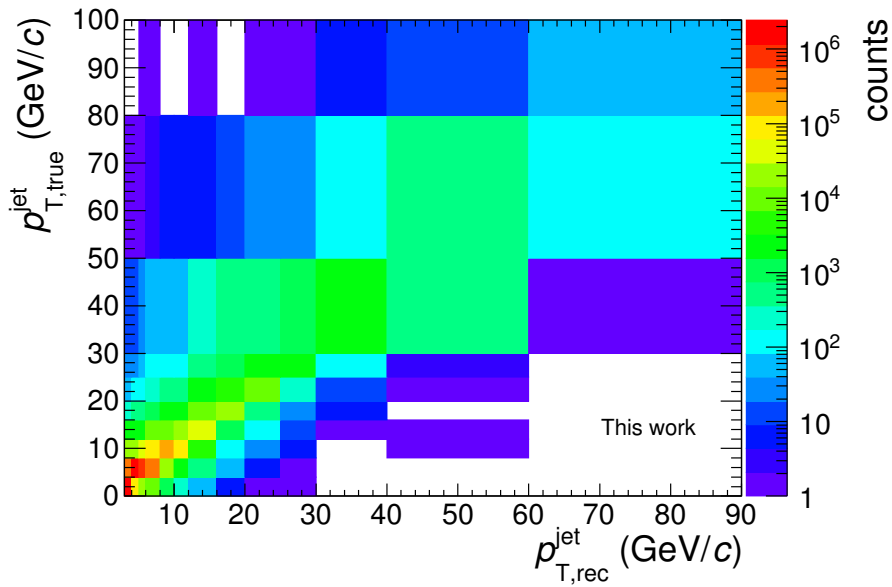


Figure 6.3: The response matrix obtained from the Monte Carlo PYTHIA 6 Perugia 11 simulation *2016j2a2* anchored to *2016l* rebinned according to (5.1) and (6.11).



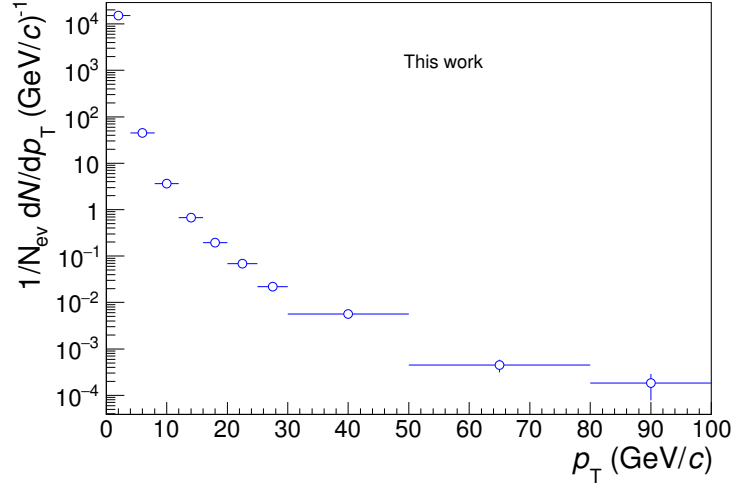


Figure 6.4: The prior distribution generated as minimum-bias, PYTHIA 8 tune 4C, p + p events at  $\sqrt{s} = 13$  TeV.

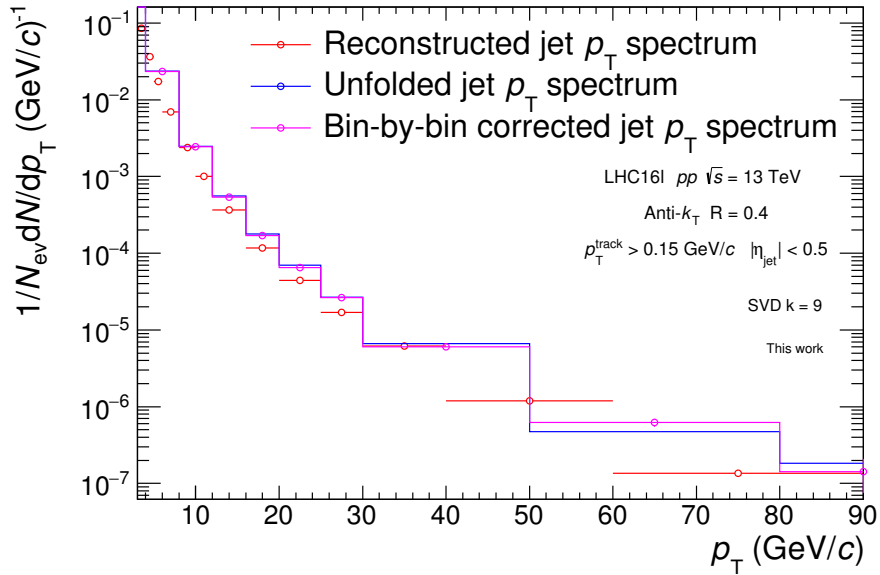


Figure 6.5: The comparison of the raw jet  $p_T$  spectrum in red, the bin-by-bin correction in magenta and the SVD-unfolded jet  $p_T$  spectrum in blue. The bin-by-bin correction has been done according to (6.12).

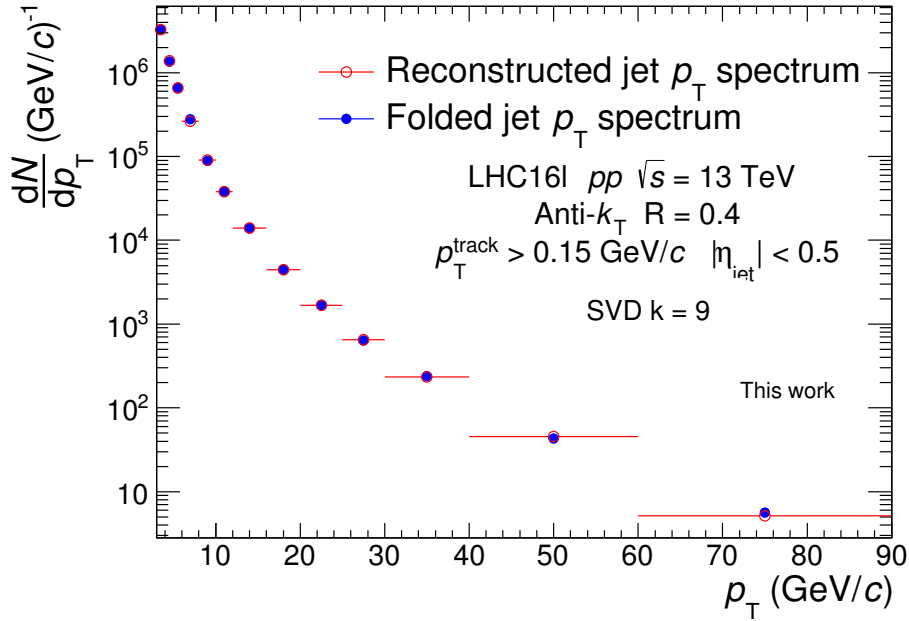


Figure 6.6: The comparison of the folded and raw jet  $p_T$  spectrum obtained from the Monte Carlo PYTHIA 6 Perugia 11 simulation *2016j2a2* anchored to *2016l*.

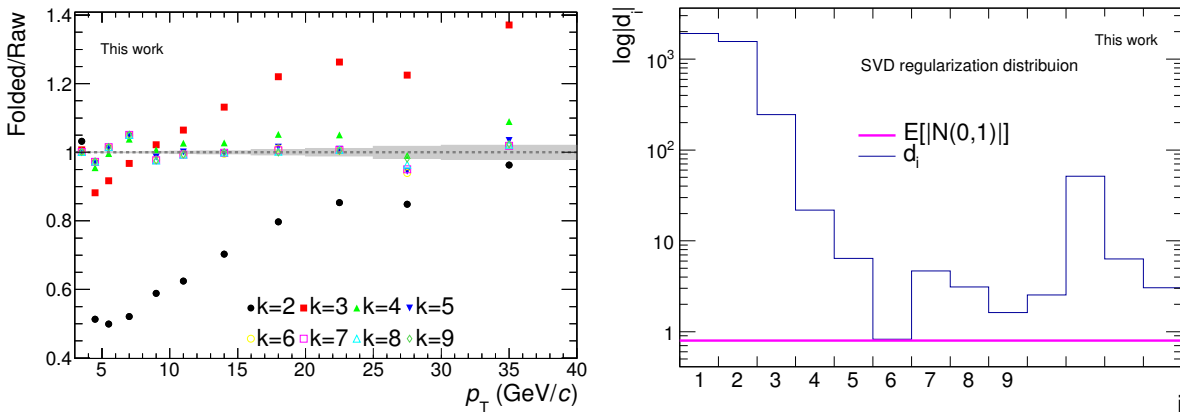


Figure 6.7: **Left:** The ratio of the folded and raw jet  $p_T$  spectra for several SVD cut-off parameters. The grey bands represent mean statistical errors of the raw jet  $p_T$  spectrum. **Right:** The  $d_i$  distribution of the SVD unfolding. The magenta line represents the expectation value  $E[|N(0,1)|]$  of the absolute normal distribution with 0 mean and a standard deviation of 1.

# Conclusion and Outlook

The thesis addresses the measurement of inclusive, charged jet spectra in p + p collisions at  $\sqrt{s} = 13$  TeV. The measured spectra were corrected for detector effects by a bin-by-bin correction and SVD unfolding. Both methods yield consistent spectra. This work documents the current state of the analysis. Its conclusions are preliminary.

The future analysis will involve

1. improving the statistics in the response matrix (it should be at least an order of magnitude higher than in the measured spectra) and the prior spectrum,
2. do a self-consistency check, i.e. a comparison of the particle level jet spectra and the unfolded spectra based on a MC simulation. This test should confirm that the unfolding procedure is consistent.
3. do the unfolding based on Bayes' theorem,
4. estimate the systematic uncertainties based on the variation of parameters of the primary analysis (the choice of binning, the spectrum range, the choice of the prior spectrum, choice of the unfolding method, the uncertainty in the smearing of  $p_T$ , the uncertainty in the tracking, the correction on the underlying event),
5. estimate the trigger efficiency and correct the number of measured events accordingly and, if the appropriate data will be available, express the measured spectrum in a cross-section,
6. the introductory chapters will be expanded by a review of the experimental results of jet measurements.



# Bibliography

- [1] Günther Dissertori, Ian Knowles, and Michael Schmelling. *Quantum chromodynamics*. Oxford University Press, 2005.
- [2] Jiří Chýla. *Quarks, partons and Quantum Chromodynamics*. Accessed: 10.09.2017.
- [3] J. Rak and M.J. Tannenbaum. *High PT Physics in the Heavy Ion Era*. Cambridge monographs on particle physics, nuclear physics, and cosmology. 2013.
- [4] Alexandre Deur, Stanley J. Brodsky, and Guy F. de Teramond. The QCD Running Coupling. *Prog. Part. Nucl. Phys.*, 90:1–74, 2016.
- [5] G. M. Prosperini, M. Raciti, and C. Simolo. On the running coupling constant in QCD. *Prog. Part. Nucl. Phys.*, 58:387–438, 2007.
- [6] Bethke and Siegfried. Experimental tests of asymptotic freedom. *Prog. Part. Nucl. Phys.*, 58:351–386, 2007.
- [7] Ringaile Placakyte. Parton Distribution Functions. In *Proceedings, 31st International Conference on Physics in collisions (PIC 2011): Vancouver, Canada, August 28-September 1, 2011*, 2011.
- [8] C. Y. Wong. *Introduction to high-energy heavy ion collisions*. 1995.
- [9] D. Ebert, R. N. Faustov, and V. O. Galkin. Mass spectra and Regge trajectories of light mesons in the relativistic quark model. *Phys. Rev.*, D79:114029, 2009.
- [10] Bo Andersson, G. Gustafson, M. Ringner, and P. J. Sutton. The Feynman-Wilson gas and the Lund model. *Eur. Phys. J.*, C7:251–261, 1999.
- [11] Torbjorn Sjostrand, Stephen Mrenna, and Peter Z. Skands. A Brief Introduction to PYTHIA 8.1. *Comput. Phys. Commun.*, 178:852–867, 2008.
- [12] Gavin P. Salam. Towards Jetography. *Eur. Phys. J.*, C67:637–686, 2010.
- [13] Yuri L. Dokshitzer, Valery A. Khoze, Alfred H. Mueller, and S. I. Troian. *Basics of perturbative QCD*. 1991.
- [14] Toichiro Kinoshita. Mass singularities of feynman amplitudes. *Journal of Mathematical Physics*, 3(4):650–677, 1962.
- [15] Matteo Cacciari, Gavin P. Salam, and Gregory Soyez. FastJet User Manual. *Eur. Phys. J.*, C72:1896, 2012.

- [16] Betty Abelev et al. Underlying Event measurements in  $pp$  collisions at  $\sqrt{s} = 0.9$  and 7 TeV with the ALICE experiment at the LHC. *JHEP*, 07:116, 2012.
- [17] Matteo Cacciari and Gavin P. Salam. Pileup subtraction using jet areas. *Phys. Lett.*, B659:119–126, 2008.
- [18] Gregory Soyez. Jet areas as a tool for background subtraction. In *25th Winter Workshop on Nuclear Dynamics (WWND 2009) Big Sky, Montana, February 1-8, 2009*, 2009.
- [19] Serguei Chatrchyan et al. Measurement of the underlying event activity in  $pp$  collisions at  $\sqrt{s} = 0.9$  and 7 TeV with the novel jet-area/median approach. *JHEP*, 08:130, 2012.
- [20] Lyndon Evans and Philip Bryant. Lhc machine. *Journal of Instrumentation*, 3(08):S08001, 2008.
- [21] LHC Guide. Mar 2017.
- [22] Cinzia De Melis. The CERN accelerator complex. Complexe des accélérateurs du CERN. Jan 2016. General Photo.
- [23] *ALICE Inner Tracking System (ITS): Technical Design Report*. Technical Design Report ALICE. CERN, Geneva, 1999.
- [24] G Dellacasa and L Ramello. *ALICE time projection chamber: Technical Design Report*. Technical Design Report ALICE. CERN, Geneva, 2000.
- [25] P Cortese, G Dellacasa, and Ramello. *ALICE forward detectors: FMD, TO and VO: Technical Design Report*. Technical Design Report ALICE. CERN, Geneva, 2004. Submitted on 10 Sep 2004.
- [26] Rüdiger Haake. Charged Jets in Minimum Bias p-Pb Collisions at  $\sqrt{s_{NN}} = 5.02$  TeV with ALICE. *PoS*, EPS-HEP2013:176, 2013.
- [27] The ALICE definition of primary particles. Jun 2017.
- [28] Andreas Hocker and Vakhtang Kartvelishvili. SVD approach to data unfolding. *Nucl. Instrum. Meth.*, A372:469–481, 1996.